CHEMISTRY OF MATERIALS

pubs.acs.org/cm Article

Tuning Point Defects by Elastic Strain Modulates Nanoparticle Exsolution on Perovskite Oxides

Jiayue Wang, Jing Yang, Alexander K. Opitz, William Bowman, Roland Bliem, Georgios Dimitrakopoulos, Andreas Nenning, Iradwikanari Waluyo, Adrian Hunt, Jean-Jacques Gallet, and Bilge Yildiz*

Cite This: *Chem. Mater.* 2021, 33, 5021−5034 Read Online

ACCESS | Metrics & More | Article Recommendations | Supporting Information

ABSTRACT: Exsolution generates stable and catalytically active metal nanoparticles via phase precipitation out of a host oxide. An ability to control the size and dispersion of the exsolution particles is desirable for design of nanostructured (electro)catalysts. Here, we demonstrate that tuning point defects by lattice strain affects both the thermodynamics and the kinetics of iron (Fe^0) exsolution on $La_{0.6}Sr_{0.4}FeO_3$ (LSF) thin film model. By combining *in situ* surface characterization and *ab initio* defect modeling, we show oxygen vacancy and Schottky defects to be the primary point defects formed upon Fe^0 exsolution. Lattice strain tunes the formation energy, and thus the abundance of these defects, and alters the amount and size of the resulting exsolution particles. In addition, we find that the density of exsolved nanoparticles matches the concentration of oxygen vacancy pairs, thus pointing to the surface oxygen vacancy pairs as preferential nucleation sites for exsolution. The tensile-strained LSF with a facile formation of these critical point defects results in a higher Fe^0 metal concentration, a larger density of nanoparticles, and a reduced particle size at its surfaces. These results provide important mechanistic insights and highlight the role of point-defect engineering in designing nanostructured catalysts in energy and fuel conversion technologies.

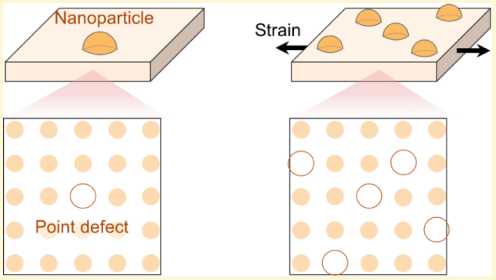

INTRODUCTION

Oxide-supported metal nanoparticles are key functional components in a wide range of energy storage and conversion technologies.[1−3] A recent advance in the design of materials for these applications is to *exsolve* metal nanoparticles that act as catalysts for reactions of interest. In this process, catalytically active transition metals are first substituted into the parent oxide under oxidizing conditions, and the metallic nanoparticles are then precipitated from the host matrix upon reduction. Nishihata et al. initially demonstrated exsolution in three-way catalysts.[4] Compared to particles prepared by deposition or impregnation,[1,5] the exsolved nanoparticles are partially embedded in the parent oxide.[6] Their anchored structure makes the exsolved nanoparticles highly resistant toward coarsening[7,8] and helps maintain the particles in their original position of nucleation.[9] In addition, the exsolved particles are more resilient against coking[6] and can be redissolved into the host oxide upon oxidation at elevated temperatures for catalyst regeneration.[10,11] Today, the concept of exsolution has been expanded to a number of other applications including solid oxide electrochemical cells,[12−14] ceramic membrane reactors,[15,16] chemical looping combustion,[17] and photocatalysis.[18] Due to the size-dependent performance of supported metal catalysts,[19] exsolved nanoparticles with ever smaller sizes and higher densities are desirable. Since exsolution often requires long-time reduction at elevated temperatures, some coarsening of particles seems to be inevitable.[8,20−22] As a result, the current exsolution studies typically report metal nanoparticles with tens of nanometers in size. To establish a desired morphology of the exsolved nanoparticles, one has to be able to control the exsolution parameters, through the underlying mechanisms.

Herein, we propose that an ability to control the point defect formation in the host oxide is needed to tune exsolution, both thermodynamically and kinetically. First, formation of oxygen vacancy and cation vacancy defects has been suggested as the elementary processes in exsolution.[23,24] Thus, the ease to form these defects in the host oxide is a key factor in the thermodynamics as well as the kinetics of exsolution. As an example, an increased concentration of A-site vacancies and oxygen vacancies in perovskite oxides (ABO_3) has been observed to assist B-site exsolution by creating local B-site excess[25] and under-coordinated B-site cations,[23,26] respectively. Second, it is known that oxygen vacancies on oxide surfaces can serve as preferential nucleation sites for supported metal nanoparticles, based on the increased binding energy of metal atom clusters to such point defects.[27,28] Using the same

Received: March 8, 2021
Revised: May 26, 2021
Published: June 15, 2021

https://doi.org/10.1021/acs.chemmater.1c00821
Chem. Mater. 2021, 33, 5021−5034

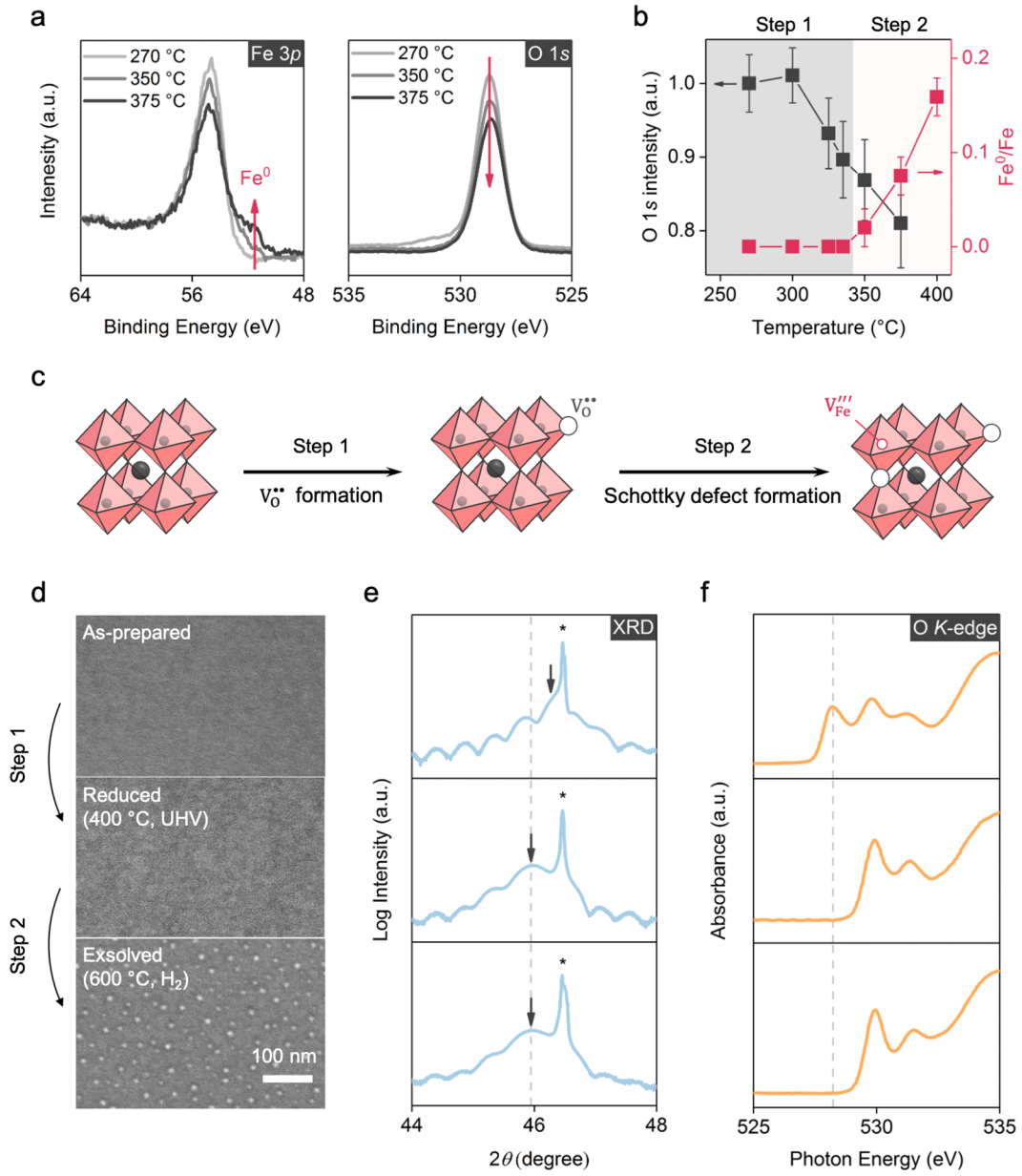

Figure 1. Chemistry and structure of LSF prior to and upon exsolution. (a) Fe 3*p* and O 1*s* spectra collected *in situ* in 0.5 Torr H_2 under different temperatures. Fe 3*p* and O 1*s* spectra were collected at a photon energy of 420 and 860 eV, respectively. (b) Evolution of surface Fe^0 concentration and the normalized O 1*s* intensity during exsolution. (c) Schematic representation of the point defect formation reactions in LSF during exsolution: first formation of oxygen vacancies, followed by the Schottky defects. (d) SEM images, (e) out-of-plane symmetric $2\theta-\omega$ XRD patterns, and (f) O *K*-edge TEY-XAS measurement of the as-prepared (top), reduced (middle), and exsolved (bottom) LSF. The XRD scan is collected at the pseudocubic (002) reflection, where LSF and $SrTiO_3$ substrate peaks are indicated with an arrow and an asterisk, respectively.

argument, we propose that oxygen vacancies can also increase the nucleation density and rate of exsolution of particles and, hence, increase the nanoparticle density and dispersion.[29]

Establishing the connection between the microscopic point defect formation and the macroscopic nanoparticle exsolution, however, is not trivial. The first challenge is to isolate point defect formation from other experimental parameters. Most studies, to date, focused on screening different host perovskite oxides and different metal cation dopants to examine the exsolution process as a function of defect concentration.[23,25] However, the large variety in the surveyed compositions introduces the uncertainty that other factors may interfere, for example, the difference in the solubility of a given metal in different perovskite hosts.[30,31] This complexity requires a method to decouple point defect formation during reduction, from other compositional effects on exsolution. Keeping the cation composition fixed while altering the concentration and stability of point defects in the host oxide by external fields is desirable for this purpose. The second challenge is to identify the key defect structure that facilitates the nucleation of exsolving particles. Previous studies have calculated the B-site segregation energy (as a metric for exsolution) as a function of defect concentration.[23,32−34] However, it remains unclear how the point defect type, structure, and distribution affect the particle nucleation process in exsolution. As noted above, oxygen vacancies may play a role here, akin to their role in

https://doi.org/10.1021/acs.chemmater.1c00821
Chem. Mater. 2021, 33, 5021−5034

binding the supported metal nanoparticles.[27,28] To address this problem, one needs to develop a method to link the local point defect chemistry and structure to the exsolution properties of the host oxide.

In this work, we present an experimental and analysis framework to tackle both of the challenges noted above. We use biaxial lattice strain as an approach to tailor point defect formation without changing the nominal cation composition of the host oxide. Previous studies have shown that lattice strain can change the concentration,[35,36] migration barrier,[37] as well as the degree of ordering[38] of point defects in oxides. Therefore, by tuning the formation energy (and thus the abundance) of the point defects in the host oxide with biaxial lattice strain, we can examine their impact on metallic nanoparticle exsolution while keeping the nominal composition of the perovskite unchanged. To quantitatively interpret the role of point defects, we developed a multiscale defect model by combining density functional theory (DFT) calculations and Monte Carlo (MC) simulations. We used the former to obtain the energetics associated with strain-dependent point defect formation, as well as binding of metal atoms to point defects, and the latter to identify the critical defect structures that facilitate nanoparticle nucleation.

To demonstrate this approach, we take epitaxial $La_{0.6}Sr_{0.4}FeO_3$ (LSF) thin films as a model system, primarily due to its well-studied defect chemistry and the range of applications that use it as an electrocatalyst.[39,40] Previous studies have demonstrated that upon reduction (both chemically[22,41] and electrochemically,[42−44] metallic iron particles (Fe^0) can be exsolved from the LSF lattice. It is known that exsolution can occur both at the surface and in the bulk of an oxide.[45,46] Recently, *in situ* transmission electron microscopy experiments have demonstrated that the metal nanoparticles nucleate directly at the surface of a perovskite oxide at early stages of exsolution.[9,17] Since the nanoparticles being exsolved on the surface are of greater importance for catalysis and electrocatalysis, we focus on the surface exsolution on LSF in this work.

By quantifying surface defect states with near-ambient pressure X-ray photoelectron spectroscopy (NAP-XPS), we identify the initial oxygen vacancy formation and the following Schottky defect formation as the primary defect reactions prior to and during Fe^0 nanoparticle exsolution on LSF. MC simulations, using *ab initio* defect and binding energies, show that oxygen vacancy pair concentration at the surface correlates well with the experimentally found nanoparticle concentration, and thus, these defect pairs could serve as nucleation sites for the exsolved Fe^0 nanoparticles. DFT calculations also confirm the oxygen vacancy pairs to be a more favorable binding site for Fe adatoms and Fe dimers, compared to isolated oxygen vacancy. Then, by tuning the formation of oxygen vacancy and Schottky defects in the LSF thin films with lattice strain, while keeping all other experimental parameters unchanged, we unequivocally demonstrate the capability to tailor nanoparticle exsolution via point defect control. As a result, the LSF surface with the most enhanced point defect formation under tensile strain had the highest Fe^0 concentration, the largest particle density, as well as the finest particle size. The strain-modified point defect formation model here can also reconcile the inconsistent strain dependencies that have been reported for exsolution on different perovskite oxides (discussed below).[47,48] Our results highlight the fundamental role of point defects in tailoring exsolution and engineering nanostructured catalysts.

RESULTS AND DISCUSSION

Point Defect Reactions Prior to and at the Onset of Exsolution. We assessed the surface defect chemistry during exsolution on the LSF film grown on $SrTiO_3(001)$ substrate using NAP-XPS. The LSF thin film was heated in 0.5 mbar of dry H_2 during continuous gas flow (Supplementary Note 1). As shown in Figure 1a, a feature at 51.5 eV in the Fe 3*p* spectra emerges at 350 °C, which can be assigned to the metallic Fe^0 species (Supplementary Note 2). The intensity of this Fe^0 species indicates the amount of Fe exsolution. Meanwhile, two changes in the normalized O 1*s* spectra arise during Fe exsolution. First, the overall intensity of the normalized O 1*s* spectra decreased upon heating in H_2 atmosphere, indicating an increase in the oxygen nonstoichiometry (δ in $La_{0.6}Sr_{0.4}O_{3-\delta}$) in the near-surface region.[49] (XPS analysis approach is presented in Supplementary Note 3.) Second, when the LSF surface is being reduced, the oxygen species at ∼532 eV, which is usually assigned to the segregated SrO surface layer of the perovskite,[50,51] vanishes. A consistent observation regarding the disappearance of the surface Sr species is present in the Sr 3d spectra (Supplementary Note 4).

The evolution of the surface Fe^0 concentration, along with the relative change in the normalized O 1*s* intensity, is plotted in Figure 1b, as a function of the reduction temperature. As illustrated, the surface chemical evolution during the exsolution process consists of two stages. First, when heating the sample in H_2 at a temperature below 350 °C, the surface became more reduced as is featured by a decrease in the O 1*s* intensity, consistent with the formation of oxygen vacancies near the surface. Meanwhile, no Fe^0 was present on the surface. In the second stage, when the reduction temperature is higher than 350 °C, Fe^0 appeared at the surface, and its concentration increase was accompanied by a further decrease in the O 1s intensity. The absolute values of the O 1*s* intensity change in Figure 1b should be treated as only semiquantitative. This is because exsolution introduces chemical and roughness evolution on the surface, making it very difficult to find a constant surface species to normalize the O 1*s* spectra. Nevertheless, the quantification uncertainties do not impede the demonstration of the increase in the oxygen nonstoichiometry during exsolution.

Based on the NAP-XPS results, we show Fe metal precipitation can only occur beyond a certain threshold of reduction. We can thus ascribe two types of point defect reactions being involved in the exsolution process (schematically shown in Figure 1c). In the first step, which we call mild reduction, the oxidized perovskite releases lattice oxygen (seen as the decrease in O 1*s* signal), forming oxygen vacancies, without reaching its critical decomposition nonstoichiometry. This step is prior to metal precipitation and can be expressed in Kröger−Vink notation[52] as

$$O_O^{\times} \rightarrow V_O^{\bullet\bullet} + 2e' + O_{atm} \quad (1)$$

where $O_O^{\times}$, $V_O^{\bullet\bullet}$, e′, and O_{atm} denote a neutral lattice oxygen, a doubly positive-charged oxygen vacancy, an electron, and an oxygen atom in the gas phase, respectively. Depending on the reducing agent, O_{atm} can be present in the form of different molecules such as O_2, H_2O, and CO_2.

In the second step, which involves metal phase precipitation, metallic Fe species form together with the oxygen release (as

https://doi.org/10.1021/acs.chemmater.1c00821
Chem. Mater. 2021, 33, 5021−5034

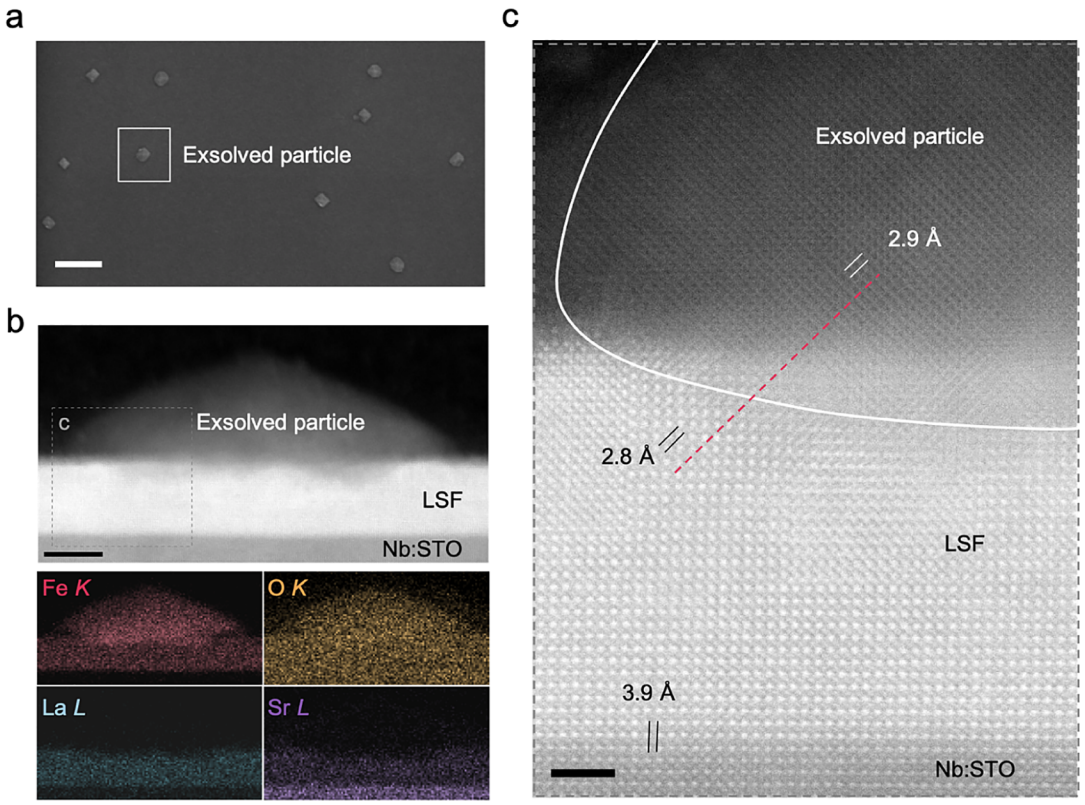

Figure 2. Atomic structure and chemical nature of the exsolved nanoparticles. (a) SEM image (scale bar: 200 nm) of an LSF film after being reduced in 200 sccm 3% H_2/N_2 at 650 °C for 5 h. (b) Low magnification high-angle annular dark field (HAADF) STEM cross-sectional image (scale bar: 10 nm) of the same sample as in (a), together with the corresponding elemental maps obtained by EDX. (c) High-resolution HAADF image (scale bar: 2 nm) of the region highlighted in (b). Note that the exsolved particle is partially embedded in the LSF thin film and forms a coherent particle/oxide interface.

revealed by the NAP-XPS measurement in Figure 1b). Upon sufficient reduction, this leads to the nucleation of metal nanoparticles. This step is associated with oxygen release and metal precipitation, resulting in the formation of $2V_{Fe}'''$-$3V_O^{\bullet\bullet}$ Schottky defects within the lattice

$$2Fe_{Fe}^{\times} + 3O_O^{\times} \rightarrow 2V_{Fe}''' + 2Fe^0 + 3V_O^{\bullet\bullet} + 3O_{atm} \quad (2)$$

where $Fe_{Fe}^{\times}$, V_{Fe}''', and Fe^0 denote a neutral Fe site, a triply negatively charged Fe vacancy, and Fe metal species, respectively. We recognize that Schottky defects can include A-site vacancies as well, but we do not have evidence to these defects that would result in the formation of La or Sr precipitation under these conditions. As presented in Figure S6, the La 4*d* and Sr 3*d* XPS spectra remained unchanged during the experiment. As such, we only considered Fe and O vacancies as a part of the Schottky defect formation process. Meanwhile, we are aware that several intermediate steps may take place in exsolution so that Fe^0 does not necessarily form directly from Fe^{3+}. For example, Fe^{3+} can be first reduced into Fe^{2+} and precipitate as iron oxide prior to Fe^0 formation. Nevertheless, since the goal of eq 2 is to describe the overall thermodynamic driving force instead of microkinetics, we keep the current format for clarity and simplicity.

We further demonstrate the role of these two defect reactions in exsolution, with a coupled chemical, morphological, and structural characterization of the LSF thin film. To begin with, we reduce the LSF film at 400 °C in ultrahigh vacuum (UHV) to mildly reduce the sample. As illustrated in Figure 1d–f, although no particles appeared on the surface during the mild reduction step, the out-of-plane lattice parameter increased by 0.6% (±0.1%) compared to the as-prepared one. This chemical expansion is induced by oxygen vacancy formation,[53] and similar lattice expansion as a result of oxygen release has also been reported for LSF powders.[54] According to the bulk chemical expansion coefficient,[40] the 0.6% lattice expansion corresponds to an increase of 0.3 in δ prior to the onset of exsolution (Supplementary Note 3). While a quantitative comparison between NAP-XPS and XRD is not possible due to the different probing depths and experimental conditions, both techniques consistently point to the increase in δ in the LSF lattice during the prereduction step. The formation of oxygen vacancies during this step is also confirmed by total electron yield mode X-ray absorption spectroscopy (TEY-XAS). In the as-prepared LSF, the pre-edge band is clearly visible in the O *K*-edge (Figure 1f). This feature is assigned to an empty state in the oxygen–iron molecular orbital—i.e., the electron hole charge compensating the Sr doping.[55] Upon reduction, the pre-edge feature completely vanishes, indicating that the hole concentration becomes negligible due to the increased oxygen deficiency in LSF.[40]

During the second step, involving more significant reduction after heating the sample to 600 °C in 80 mTorr H_2, the particles started to appear on the surface, as seen in Figure 1d. Since there is metal precipitation at this step, this has to be associated with Schottky defect formation within the lattice (eq 2). Nevertheless, no apparent lattice volume change could be detected with the XRD measurement during this step, as

https://doi.org/10.1021/acs.chemmater.1c00821
Chem. Mater. 2021, 33, 5021−5034

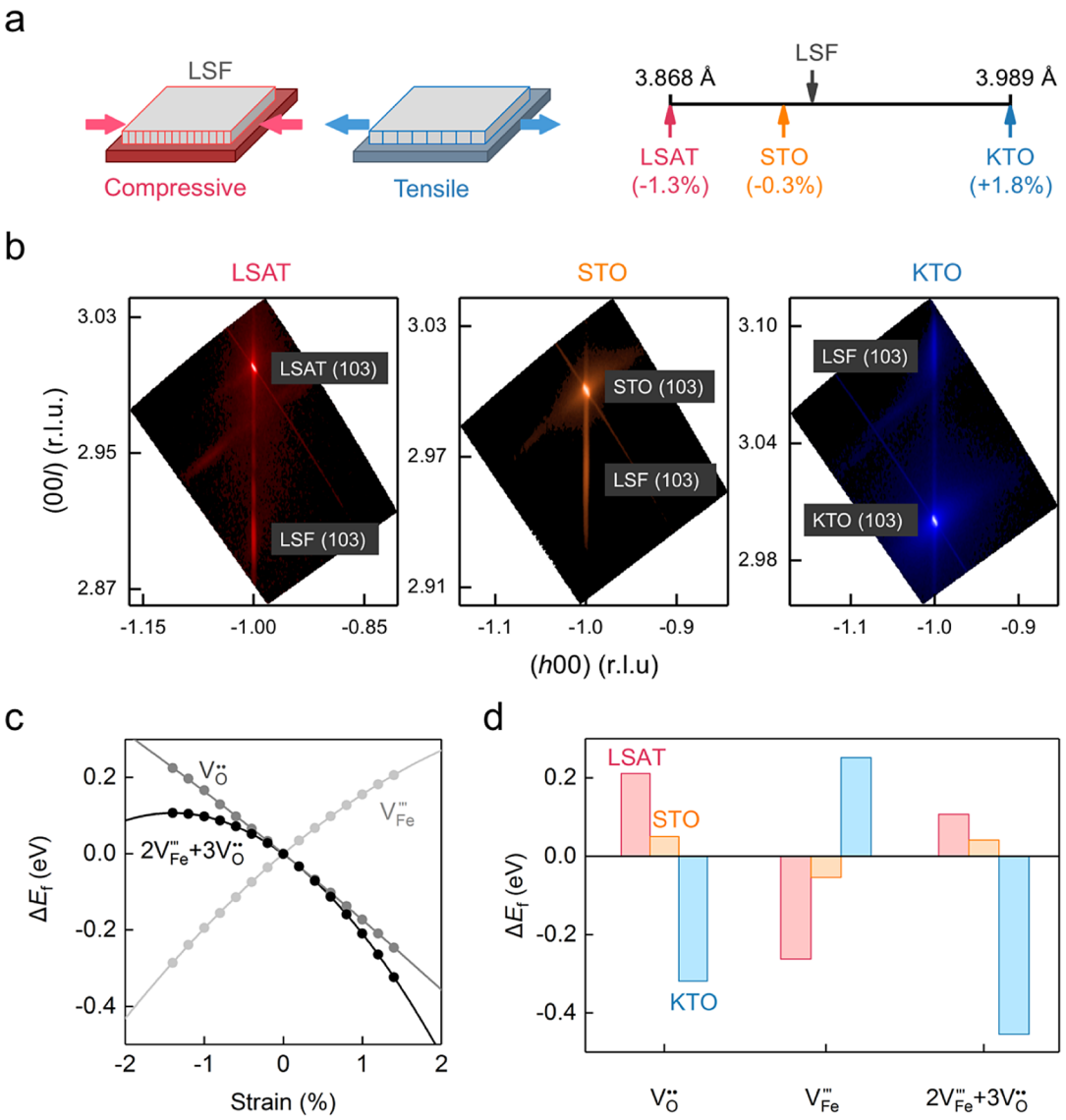

Figure 3. Tuning point defect formation in the LSF thin films with biaxial lattice strain. (a) Schematic representation depicting the sample geometry, where biaxial lattice strain is introduced by heteroepitaxy. The number of lines indicates the range of in-plane strains achieved in LSF. Here, the tensile strain is denoted as positive, and compressive strain as negative. (b) X-ray RSM about the (103) reflection of coherently strained LSF thin films, collected after the exsolution test. Note the film peaks are directly below or above that of the substrate, confirming identical in-plane lattice constants and that the epitaxy is preserved after this exsolution process. (c) Change in the defect formation energy for the oxygen vacancy, iron vacancy, and the Schottky defect versus biaxial lattice strain. The data points are calculated by DFT, while the lines represent the parabolic fits. The zero reference point corresponds to the unstrained state. Note that tensile strain facilitates the formation of both the oxygen vacancy and the Schottky defect. (d) Calculated defect formation energy difference at the nominal strain values of the differently strained LSF films. The unit cell used in the DFT calculation is described in Supplementary Note 7.

indicated by the dashed line in Figure 1e. This may arise from two possible scenarios: counteraction of cation and anion vacancy formation on the lattice volume, as cation vacancies contract the lattice while oxygen vacancies expand it;[56,57] and a nonuniform distribution of Schottky defects that is confined to the near-surface region under diffusion-limited conditions (Supplementary Note 5). In addition, we did not observe diffraction peaks for metallic iron and $LaSrFeO_4$ in the exsolved LSF film—the two characteristic phases for fully decomposed LSF thin films.[58,59] These observations indicate that the LSF films investigated in this work were at early stages of surface exsolution, prior to bulk metal precipitation (decomposition).[60]

The structure and chemical composition of the exsolved nanoparticles were further investigated by aberration-corrected scanning transmission electron microscopy (STEM) imaging and energy-dispersive X-ray spectroscopy (EDX). To facilitate the STEM specimen preparation, large exsolved nanoparticles are needed, and so the LSF film was exsolved in a harsh reducing environment (3% H_2/N_2, 650 °C, see Methods for details) prior to STEM. As a result, the nanoparticles in the STEM imaging were larger than the other nanoparticles presented in this work, which were imaged right after the exsolution onset. The planar and cross-sectional views of the exsolved LSF film are presented in Figure 2a,b, respectively. While exsolution can occur both at the surface and in the bulk of the host oxide,[45,46] only surface exsolution was observed in

https://doi.org/10.1021/acs.chemmater.1c00821
Chem. Mater. 2021, 33, 5021−5034

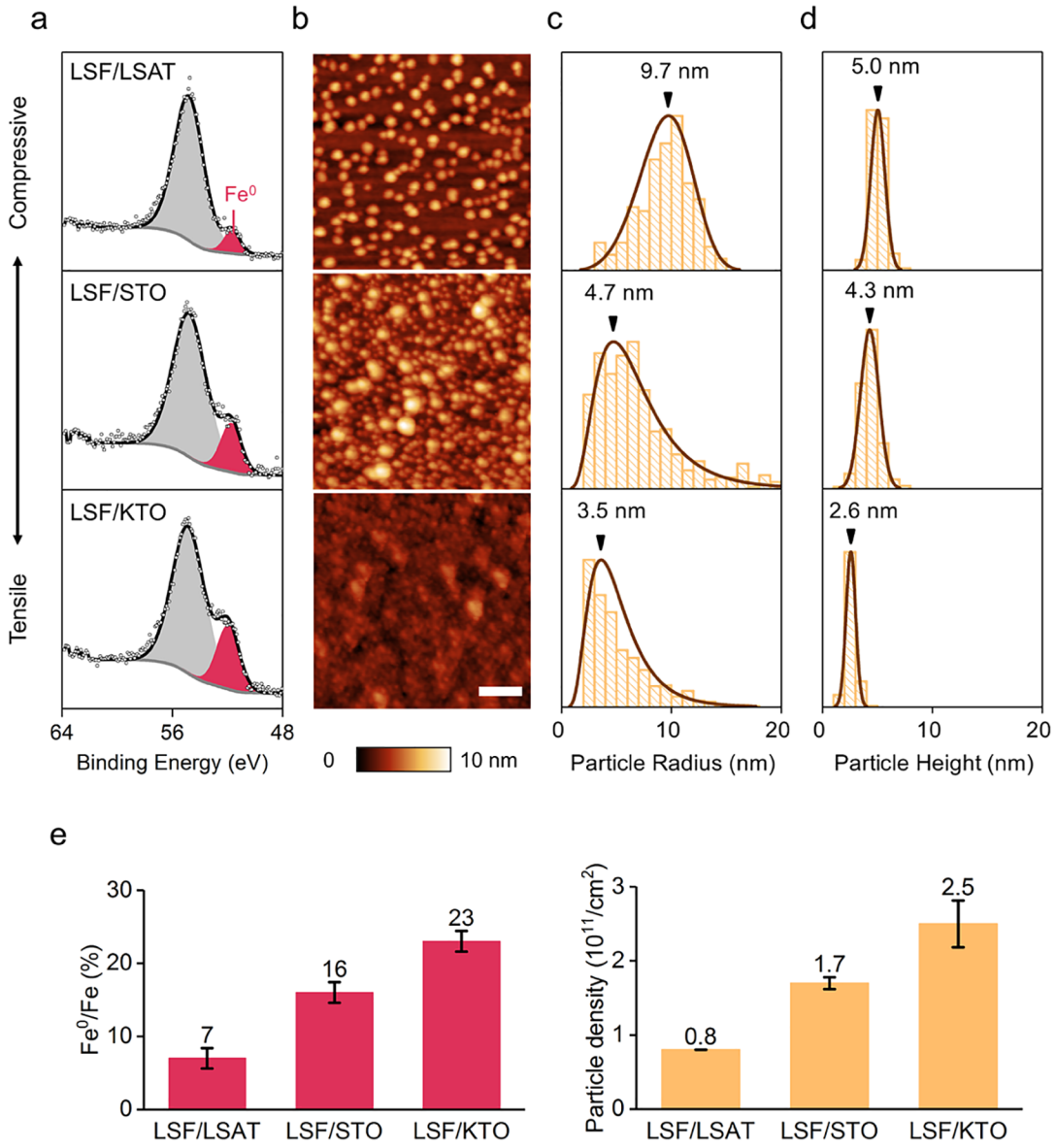

Figure 4. Comparison of Fe^0 exsolution on the LSF thin films with strain-modulated point defect formation. (a) Comparison of *in situ* Fe 3*p* spectra at 400 °C in 0.5 mbar H_2, where the LSF film under tensile strain (LSF/KTO) demonstrated the largest Fe^0 feature. (b) *Ex situ* AFM images showing the surface morphology after exsolution (scale bar: 100 nm), together with histograms of the (c) equivalent disk radius and (d) average height of the nanoparticles on the surface. From in-plane compression to tension, there is a clear decrease in both height and radius of the surface particles. (e) Surface Fe^0 concentration and particle density on the differently strained LSF thin films after exsolution. LSF films under tensile strain demonstrated the highest particle density as well as the largest $[Fe^0]$ at the surface upon exsolution.

this study. Assuming that the Fe vacancies are uniformly distributed in the entire film, the nanoparticles shown in Figure 2a correspond to only about ~1% Fe vacancy in LSF. In addition, the particles are partially embedded into the LSF surface. As discussed in the Introduction section, this "anchored" structure is a typical characteristic of exsolved nanoparticles.[6] The elemental mapping reveals that the surface nanoparticle is composed of Fe and O. Remarkably, as indicated by the red dashed line in Figure 2c, the exsolved nanoparticle formed a coherent interface with its parent oxide. The highlighted atomic spacing of the particle represents the *d*-spacing of the (220) planes of Fe_3O_4 (space group $Fd\bar{3}m$), which demonstrates the $(220)_{LSF}//(220)_{Fe_3O_4}$ crystalline orientation relation at the interface. Based on the *in situ* NAP-XPS characterization (Figure 1) and thermodynamics analysis (Supplementary Note 1), we expect the surface nanoparticles to be initially exsolved as metallic iron nanoparticles. However, the surface particles were oxidized[41] in air during the STEM sample preparation, which explains the iron oxide observed in the STEM characterization instead of metallic iron. This observation highlights the importance of employing *in situ* characterization tools such as NAP-XPS to investigate the exsolution process.

Tuning Exsolution with Strain-Modified Point Defect Formation. The abovementioned results demonstrate that $V_O^{\bullet\bullet}$ and Schottky defect formations are the two primary point defect reactions (eqs 1 and 2, which take place prior to and during exsolution, respectively. As a result, the ease to form these two defects in the oxide lattice thermodynamically determines the onset of exsolution. In this section, we demonstrate the capability to tailor Fe^0 exsolution on LSF by

https://doi.org/10.1021/acs.chemmater.1c00821
Chem. Mater. 2021, 33, 5021−5034

tuning the formation energy of these two defects with a biaxial lattice strain.

As sketched in Figure 3a, the lattice strain is introduced by growing the LSF films epitaxially onto the three (001)-oriented perovskite-type single crystal substrates with different lattice parameters: $La_{0.18}Sr_{0.82}Al_{0.59}Ta_{0.41}O_3$ (LSAT), $SrTiO_3$ (STO), and $KTaO_3$ (KTO). These three LSF films are denoted with LSF/LSAT, LSF/STO, and LSF/KTO, respectively. The in-plane lattice strain ε of the LSF films is defined as

$$\varepsilon = \frac{\Delta a}{a_0} \tag{3}$$

where a_0 represents the strain-free lattice parameter, and Δa indicates the change in lattice parameter due to substrate clamping. To verify the film epitaxy during the exsolution experiment, X-ray diffraction reciprocal space maps (RSMs) were collected after Fe exsolution. As depicted in Figure 3b, the film peaks are directly below or above that of the substrate, meaning that the LSF thin films maintained identical in-plane lattice parameters as that of the substrates even after exsolution. The RSM measurement, thus, verifies that the LSF films were coherently strained during the entire exsolution process. As discussed in Supplementary Note 6, the strains introduced by lattice clamping (eq 3) are much larger than the thermal strains during exsolution. As a result, the overall elastic strain for the three samples at the exsolution condition (400 °C) is expected to be −1.34% (LSF/LSAT), −0.34% (LSF/STO), and +1.66% (LSF/KTO). Therefore, the three samples used in this work clearly represent the LSF films with three different strain states during exsolution: compressive, nearly stress-free, and tensilefor LSF/LSAT, LSF/STO, and LSF/KTO, respectively.

To illustrate how the point defect formation energy in LSF is modulated by the biaxial lattice strain, we used DFT to calculate the defect formation energy in LSF as a function of lattice strain. A slightly different composition ($La_{0.5}Sr_{0.5}FeO_3$) was chosen in the DFT calculation to reduce the size of the simulation cell and minimize the calculation time needed. Consistent with experimental samples, the cell is strained in-plane and fully relaxed in the out-of-plane direction (Supplementary Note 7). As a result of these calculations, we find that oxygen vacancy formation in the 2 × 2 × 2 LSF unit cell expands the lattice by ∼2%, while an Fe vacancy alone contracts the lattice by ∼2%. Consistent with their volume change, the formation energies of these two defects behave oppositely under strain. As shown in Figure 3c, tensile strains reduce the formation energy of $V_O^{\bullet\bullet}$ but increase the formation energies for V_{Fe}'''. Assuming noninteracting defects as a first-order approximation, we estimate the strain dependency of the formation of the $2V_{Fe}'''$-$3V_O^{\bullet\bullet}$ Schottky defect (cf. eq 2) by a linear combination of the individual $V_O^{\bullet\bullet}$ and V_{Fe}'''. As a result, the formation energy of the $2V_{Fe}'''$-$3V_O^{\bullet\bullet}$ Schottky defect decreases under tensile strain; thus, tensile strain makes it easier to form and stabilize this type of defect that triggers exsolution of metal precipitates.

Figure 3d compares the relative change in the defect formation energy at the nominal strain values of the LSF/LSAT, LSF/STO, and LSF/KTO films. Here, the zero reference point corresponds to the unstrained state and negative ΔE_f values indicate favorable defect formation. The formation energy of both $V_O^{\bullet\bullet}$ and the $2V_{Fe}'''$-$3V_O^{\bullet\bullet}$ Schottky defect decreases from LSF/LSAT to LSF/STO and to LSF/KTO. In other words, tensile strain could facilitate both the prereduction reaction (eq 1) and the Schottky reaction (eq 2), i.e., the two essential steps of exsolution in the LSF films. As a result, we would expect the tensile-strained LSF/KTO sample to exhibit the most enhanced exsolution among the three LSF samples.

To test this hypothesis, we compared the exsolution behavior of the three differently strained LSF thin films. Since LSF is expected to completely decompose over time in pure H_2, we did not focus on the equilibrated state of these films. Instead, we compared the surface chemistry and morphology of these films consistently after 0.5 h reduction in 0.5 mbar H_2 at 400 °C. As shown in Supplementary Note 8, the as-prepared differently strained LSF films have similar surface cation chemistry and morphology. After Fe exsolution, a clear strain-dependent surface morphology and chemistry were observed on these samples (Figure 4). Consistent with our computational predictions, the tensile-strained LSF/KTO sample exhibited the most enhanced exsolution outcome. First, *in situ* Fe 3*p* spectra reflect an increase in the surface concentration of metallic iron [Fe^0] from in-plane compression to tension (Figure 4a). Second, strain-dependent morphology was also observed on the same samples (Figure 4b). To better visualize the difference in the morphology, histograms of the equivalent disk radius as well as average height of these nanoparticles were generated from the images and are presented in Figure 4c,d. As illustrated, the mode value (Figure 4c) of the equivalent particle radius decreases from compressive to tensile strain: while the particles on the surface of LSF/LSAT have a mode radius of ∼10 nm, LSF/KTO generated finer particles with a mode radius of around 4 nm. Similar trends can also be observed for the average particle height (Figure 4d), which also decreases with the increase in the tensile strain.

Please note that due to the particle oxidation by the atmosphere (Figure 2), the *ex situ* atomic force microscopy (AFM) results shown in Figure 4 may overestimate the real particle size. In addition, due to the tip convolution effects,[61] the apparent topography in AFM scans can differ from the real particle morphology. In particular, the particles on the LSF/KTO surface are approaching the AFM resolution limit[62] (Supplementary Note 9). Nevertheless, by comparing the AFM resolution limit with the mode particle size and by examining the surface morphology with different AFM tips, we can safely exclude artifacts being responsible for the observed trends. As an additional support, we observed similar strain-dependent exsolution in LSF when reducing the thin-film samples in a UHV chamber at higher temperatures (Supplementary Note 10).

As summarized in Figure 4e, these findings clearly demonstrate that, even with the same bulk cation chemistry and the same reduction conditions, tuning point defect formation of LSF can significantly modulate its exsolution behavior. That is, we expect the tensile-strained LSF to have the highest surface Fe^0 concentration, the largest particle density, as well as the finest particle size after exsolution. It should also be noted that, although the surface catalytic activity of these strained films was not examined in this work, this can be inferred from the previous work. First, it has been demonstrated that the surface catalytic activity of LSF increases with surface [Fe^0] when LSF was used as a cathode for H_2O splitting.[63] Moreover, it is also known from other catalytic studies that smaller metal nanoparticles increase the

https://doi.org/10.1021/acs.chemmater.1c00821
Chem. Mater. 2021, 33, 5021−5034

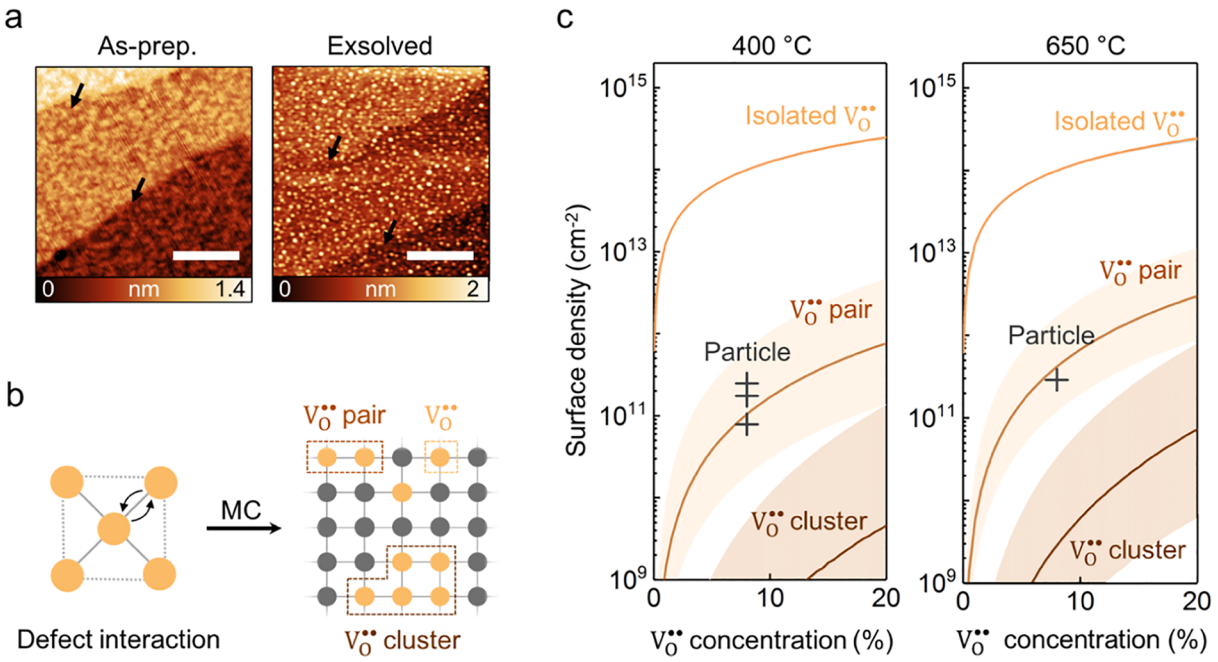

Figure 5. Correlation of Fe^0 nanoparticle exsolution with $V_O^{\bullet\bullet}$ pair formation. (a) AFM images of an atomically flat LSF(001) thin film before and after exsolution (same sample, different imaging spots). The arrows indicate the locations of the atomic steps. Scale bars: 200 nm. (b) Illustration of the defect model for the LSF(001) oxygen sublattice. The $V_O^{\bullet\bullet}$ and O^{2-} sites are colored by orange and gray in the 2D cubic lattice, respectively. Two $V_O^{\bullet\bullet}$ sites are considered to be in the same defect complex if they are nearest neighbors in a vacancy cluster. (c) Calculated surface densities of the isolated $V_O^{\bullet\bullet}$, $V_O^{\bullet\bullet}$ pairs, and $V_O^{\bullet\bullet}$ clusters on the LSF(001) surface at 400 and 650 °C as a function of total $V_O^{\bullet\bullet}$ concentration taken as a variable at the surface. The solid lines are obtained with a neighboring $V_O^{\bullet\bullet}$–$V_O^{\bullet\bullet}$ interaction energy of 0.3 eV, while the shaded region indicates the uncertainty in the defect modeling, which is calculated by changing the interaction energy by ±0.1 eV. The scattered data points represent the experimentally observed iron particle density in Figures 4b and 5a. Note that the exsolved Fe^0 nanoparticle densities fall well within the range of the computed surface $V_O^{\bullet\bullet}$ pair density.

rate of various chemical reactions either by increasing the effective surface area per volume or by increasing the intrinsic reactivity of the catalyst material itself.[2,19,64] Therefore, with the highest [Fe^0] and smallest particle size on LSF/KTO, we anticipate the tensile-strained LSF to have the highest surface catalytic activity.

Discussion on Strain Dependencies of Nanoparticle Exsolution. Prior to this work, there have been conflicting reports regarding the dependence of exsolution on strain in perovskite oxides. For example, Kim et al.[47] reported tensile strain to promote Co exsolution in $SrTi_{0.75}Co_{0.25}O_3$ (STC). On the contrary, Han et al.[48] reported that compressive strain facilitated Ni exsolution in $La_{0.2}Sr_{0.7}Ti_{0.9}Ni_{0.1}O_3$ (LSTN). These studies suggest that the strain dependency can be system-dependent and the underlying mechanism still needs to be explored and discussed. As will be elaborated below, these seemingly contradictory observations can be reconciled within the framework proposed in this work in terms of point defect formation.

In the work by Kim et al.,[47] the authors interpret the strain dependence of exsolution based solely on the Co (B site) vacancy formation that becomes easier under tensile strain. Their analysis misses a key step in exsolution; that is, the reduction in the lattice itself. While Co vacancy formation is a part of the process, it is not the only, and certainly not the first, defect to be involved. Critically, one has to also consider the reduction of the metal cations in the oxide via oxygen vacancy formation. This is because B-site vacancies do not form independently in the host oxide during exsolution but rather form together with oxygen vacancies as Schottky defect. Moreover, a threshold of oxygen nonstoichiometry also needs to be obtained in the lattice prior to the onset of exsolution. As a result, oxygen vacancy and Schottky defect should be the two fundamental point defects that determine the thermodynamics for exsolution, not the B-site vacancy alone. This point can be further supported by our observations for Fe^0 exsolution in LSF: while the formation of Fe vacancy is more favorable under lattice compression (Figure 3c), the overall exsolution phenomenon was boosted with lattice tension (Figure 4 and Supplementary Note 10). As both Co vacancy and oxygen vacancy formation are easier in STC under tensile strain,[47] we can infer that tensile strain facilitates both the prereduction reaction (eq 1) and the Schottky reaction (eq 2) in STC, too. This explains the enhanced exsolution of Co on tensile-strained STC, similar to the LSF case reported in this work.

However, Han et al.'s work on LSTN, which shows more exsolution under compressive strain, does not explicitly consider the role of any point defects.[48] Nevertheless, we can estimate the strain dependency of point defects and the resulting exsolution in that material system, too, based on defect formation volume and strain energy. Since a point defect formation can result in lattice expansion or contraction,[53] the overall lattice volume often changes after the exsolution reaction (Supplementary Note 11). Conversely, the expanded/contracted lattice volume imposed facilitates or impedes the formation of point defects.[56] Thus, we expect that introducing tensile strain to the host oxide facilitates the formation of the defect(s) formed upon exsolution, if that oxide lattice expands after exsolution, and vice versa. For the case of LSF, lattice expands during exsolution (Figure 1e) so that applying a tensile strain to this material facilitates the formation of both oxygen vacancies and Schottky defects and results in more

https://doi.org/10.1021/acs.chemmater.1c00821
Chem. Mater. 2021, 33, 5021−5034

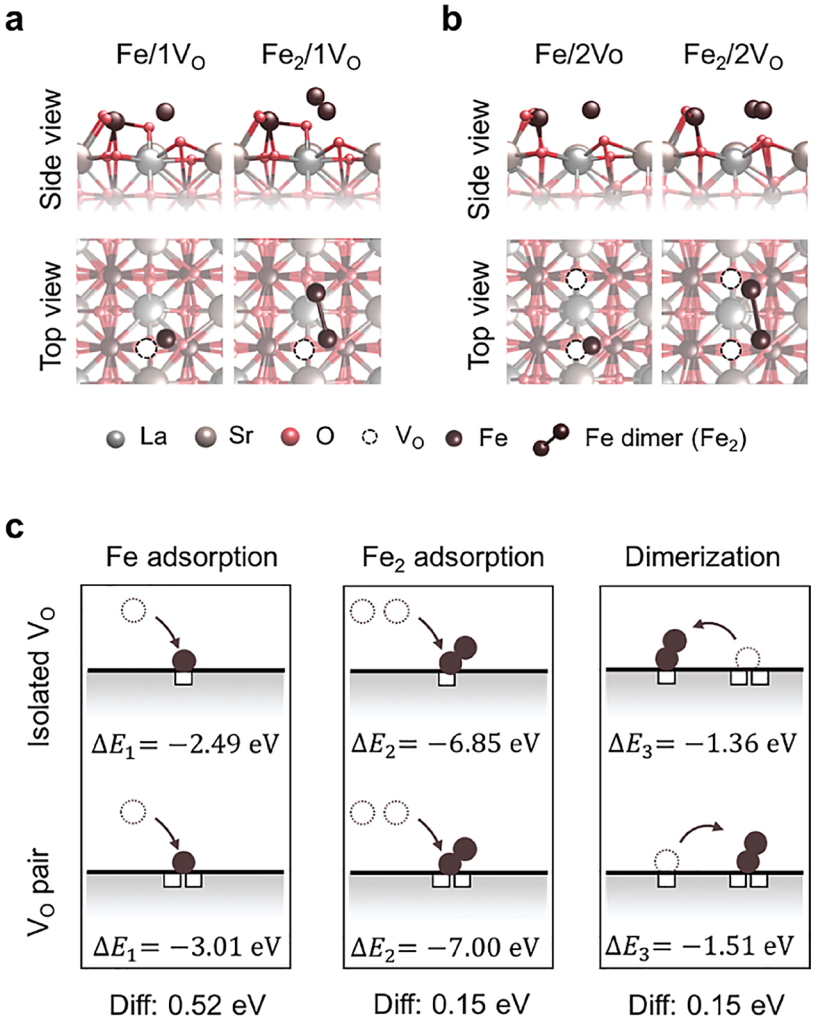

Figure 6. Effect of oxygen vacancy on adsorption of Fe atoms and Fe_2 dimers. (a and b) Fe and Fe_2 dimer structures on (a) isolated $V_O^{\bullet\bullet}$ sites ($1V_O$), and (b) $V_O^{\bullet\bullet}$ pair ($2V_O$) sites of the FeO_2-terminated LSF(100) surface. (c) Comparison of the Fe adsorption, Fe_2 adsorption, and Fe dimerization energies on isolated $V_O^{\bullet\bullet}$ and $V_O^{\bullet\bullet}$ pairs. The energy differences (Diff.) for these two types of adsorption sites are summarized at the bottom of each panel. As illustrated, all three processes are more favored on $V_O^{\bullet\bullet}$ pairs compared to on the isolated $V_O^{\bullet\bullet}$.

facile exsolution. However, the LSTN lattice contracted after Ni exsolution in Han's work,[48] indicating that the point defects involved in the exsolution reaction contract the lattice. Based on the above thoughts, we thus expect compressive strain to facilitate Ni exsolution in LSTN, which is consistent with the finding in ref 48.

Therefore, we can reconcile all these works, LSF in this report and LSTN and STC in refs 47 and 48, by considering the coupling of point defects involved in exsolution to the strain energy of the thin films. The favored strain tensor to promote nanoparticle exsolution in all the systems represent the one that favors the formation of the defects responsible for exsolution of metal particles out of the host oxide—in LSF, we have shown these defects to be oxygen vacancy and Schottky defects that are favored under tensile strain.

$V_O^{\bullet\bullet}$-Mediated Nanoparticle Nucleation. To date, several studies analyzed the nanoparticle exsolution based on the homogeneous nucleation theory.[48,65] In this section, we show that a heterogeneous nucleation model can be more appropriate to describe exsolution because nucleation of the metal particles can preferentially take place on defect sites at the surface. To do so, we investigated the morphological evolution of an atomically smooth LSF(001) thin film during Fe^0 exsolution. The film was exsolved by thermal reduction in the UHV chamber (base pressure = 10^{-9} mbar), where the Fe^0 exsolution was confirmed with *in situ* lab-based XPS. The *ex situ* AFM images of the LSF surfaces before and after exsolution are shown in Figure 5a. As illustrated, the as-prepared LSF thin film has flat terraces that are separated by monolayer atomic steps (Supplementary Note 12). After heating the LSF sample to 650 °C in UHV, nanoparticles started to form on the surface, together with the appearance of Fe^0 species in the Fe 2*p* photoelectron spectra (Supplementary Note 12). One important feature to note in Figure 5a is that the exsolved nanoparticles are uniformly distributed on the terraces, with no preference to the step edges. This characteristic suggests that certain defect sites at the surface are more favorable for nanoparticle nucleation and growth than step edges.[27,28]

As discussed in the Introduction section, we hypothesize that this preferential nucleation site is related to the surface oxygen vacancies. This is because both isolated and clustered $V_O^{\bullet\bullet}$ sites have been shown as favorable nucleation sites for metal particle growth on binary oxides.[66−68] We cannot visually probe the nucleation sites on the LSF surface at the exsolution onset. We can, instead, correlate the concentration

https://doi.org/10.1021/acs.chemmater.1c00821
Chem. Mater. 2021, 33, 5021−5034

of oxygen vacancies to the concentration of Fe^0 nanoparticles as an indirect measure to test this hypothesis. Since the exsolved particles are anchored and maintain their nucleation position,[9] we expect that the observed particle density largely reflects the density of the nucleation sites at the exsolution onset. Hence, a direct comparison between the Fe^0 nanoparticle density and the surface concentration of different types of defect structures can be useful in identifying the nature of the nucleation center.

Motivated by this idea, we combined DFT and MC simulations to model the microscopic defect structure of the LSF surface. The defect model takes into account the stability of both individual oxygen vacancies and their interacting pairs (clusters), as schematically shown in Figure 5c. First, we construct a 2D cubic lattice with periodic boundary conditions to represent the LSF(001) surface as experimentally observed (Supplementary Note 12). In this simulated 2D lattice, each element represents either a surface oxygen atom or a $V_O^{\bullet\bullet}$. Then, a model Metropolis MC simulation was conducted on this 2D lattice to simulate the process of defect clustering. The simulation temperatures were set to match the experimental exsolution condition in Figures 4 and 5. The interaction energy between the first nearest neighbor (1NN) $V_O^{\bullet\bullet}$ sites is 0.3 ± 0.1 eV, with positive value representing repulsion. This interaction energy comes from our DFT calculations of vacancy−vacancy interactions on the FeO_2-terminated LSF(001) surface. Finally, the concentrations of isolated $V_O^{\bullet\bullet}$, nearest-neighbor $V_O^{\bullet\bullet}$ pairs, and $V_O^{\bullet\bullet}$ clusters were calculated from the thermodynamically equilibrated lattices. Here, we define $V_O{}^{\bullet\bullet}$ clusters as any $V_O{}^{\bullet\bullet}$ complexes that contain more than two oxygen vacancies.

Figure 5c shows the surface density of the isolated $V_O^{\bullet\bullet}$, $V_O^{\bullet\bullet}$ pairs, and $V_O^{\bullet\bullet}$ clusters on the equilibrated oxygen sublattice as a function of surface oxygen deficiencies ($V_O^{\bullet\bullet}$ concentration) at 400 and 650 °C. As illustrated, due to the $V_O^{\bullet\bullet}-V_O^{\bullet\bullet}$ repulsion, the surface defect density follows isolated $V_O^{\bullet\bullet} \gg V_O^{\bullet\bullet}$ pairs $\gg V_O^{\bullet\bullet}$ clusters for both temperatures. Meanwhile, due to the increased thermal energy (k_BT), the equilibrated $V_O^{\bullet\bullet}$ pairs and $V_O^{\bullet\bullet}$ clusters are higher at 650 °C than at 400 °C. In the same plot, the nanoparticle densities on the exsolved LSF surfaces (Figures 4b and 5a) are plotted at $[V_O^{\bullet\bullet}]$ = 8%, the critical oxygen nonstoichiometry prior to the exsolution onset (Supplementary Note 3). By comparing the surface density of the exsolved Fe^0 nanoparticle and that of the $V_O^{\bullet\bullet}$-related point defects, we found that the measured particle density falls well within the range of the calculated $V_O^{\bullet\bullet}$ pair concentration. However, the calculated density of both the individual $V_O^{\bullet\bullet}$ sites and the large $V_O^{\bullet\bullet}$ clusters are around 3 orders of magnitude off compared to the particle density. This comparison delivers a strong evidence that $V_O^{\bullet\bullet}$ pairs are more likely to be the nucleation site for Fe^0 nanoparticle exsolution on the LSF surface, rather than individual $V_O^{\bullet\bullet}$ sites and large $V_O^{\bullet\bullet}$ clusters.

To assess the validity of this correlation at the atomic level, we examine whether Fe prefers to nucleate on the $V_O^{\bullet\bullet}$ pairs. Since metal dimer formation can constitute the first step in metal nanoparticle nucleation,[69] we calculated the Fe dimer formation on the FeO_2-terminated LSF(001) surface using DFT. Figure 6a,b shows the configuration of the adsorbed Fe and Fe_2 dimers at isolated $V_O^{\bullet\bullet}$ and $V_O^{\bullet\bullet}$ pairs. Based on these configurations, we calculated three characteristic energies associated with Fe dimer (Fe_2) formation: Fe adsorption energy ΔE_1, Fe dimer adsorption energy ΔE_2, and the Fe dimerization energy ΔE_3. These energies are defined as follows:

$$\Delta E_1(S_{LSF}) = -E(Fe/S_{LSF}) + E(Fe) + E(S_{LSF}) \quad (4)$$

$$\Delta E_2(S_{LSF}) = -E(Fe_2/S_{LSF}) + 2 \times E(Fe) + E(S_{LSF}) \quad (5)$$

$$\Delta E_3(S_{LSF}) = -E(Fe_2/S_{LSF}) - E(S'_{LSF}) + E(Fe/S_{LSF}) + E(Fe/S'_{LSF}) \quad (6)$$

where S_{LSF} and S'_{LSF} indicate the different adsorption sites on the LSF surface, which can be either an isolated $V_O^{\bullet\bullet}$ or a $V_O^{\bullet\bullet}$ pair. ΔE_1 and ΔE_2 measure the capability to bind an Fe adatom and an Fe_2 dimer to a given site on the LSF surface. Meanwhile, the Fe dimerization energy ΔE_3 measures the stability of the adsorbed Fe_2 dimer on a given site with respect to two separate Fe adatoms that are bound to an isolated $V_O^{\bullet\bullet}$ and a $V_O^{\bullet\bullet}$ pair, respectively.

These three characteristic energies for the isolated $V_O^{\bullet\bullet}$ and $V_O^{\bullet\bullet}$ pairs, together with the energy difference between these two types of adsorption sites, are summarized in Figure 6c. As shown, Fe and Fe_2 adsorption are favored on the $V_O^{\bullet\bullet}$ pairs by 0.52 and 0.15 eV. Based on the equilibrium of two-level systems, we expect more than 99% of the Fe adatoms and more than 80% of Fe_2 adsorbates to occupy the $V_O^{\bullet\bullet}$ pairs instead of the isolated $V_O^{\bullet\bullet}$ sites at the exsolution conditions (Supplementary Note 13). The DFT calculation thus confirms that $V_O^{\bullet\bullet}$ pairs are more favorable to form Fe adatoms and Fe dimers on the LSF surface, compared to the isolated $V_O^{\bullet\bullet}$ sites. As a result of these MC simulations and DFT calculations, we can anticipate that the $V_O^{\bullet\bullet}$ pairs formed during the prereduction step to be a critical defect structure responsible for the nanoparticle nucleation in exsolution. Assuming noninteracting defects as a first-order approximation, we estimate the strain dependency of oxygen vacancy pair formation to be similar to that of individual $V_O^{\bullet\bullet}$ (Figure 3). As a result, tensile strain should also facilitate the formation of oxygen vacancy pairs in LSF. As a support of this argument, we note that strain-enhanced oxygen vacancy pairing/ordering has also been observed in previous studies.[36,38]

While further studies are required to illustrate the detailed nucleation mechanism, some practical insights can be already extrapolated from this work. Prior observations have shown that grain boundaries[8,70] can act as preferential nucleation sites for the exsolved nanoparticles. It is reasonable that on polycrystalline specimens, grain boundaries act as nucleation sites for the exsolved nanoparticles.[71] However, for those grain-boundary-facilitated nucleation scenarios, the particle density is much smaller ($\sim 10^9$ cm^{-2}) compared to the ones in this work ($\sim 10^{11}$ cm^{-2}). Therefore, promoting point-defect-mediated nucleation may be even more important than engineering grain boundaries in the host oxide to enhance the exsolution process. As a result, we expect oxygen vacancy engineering to be an effective approach to tailor the particle density in nanoparticle exsolution.

CONCLUSIONS

In summary, using lattice strain to tune the point defect formation in a model perovskite oxide system, we demonstrate the capability to tailor nanoparticle exsolution using elastic strain and point defect engineering. We quantitatively measured the fundamental role of oxygen vacancy and Schottky defect formation in both the thermodynamics and the nucleation kinetics of Fe^0 nanoparticle exsolution in epitaxial thin-film LSF. Tensile strain favors the formation of

https://doi.org/10.1021/acs.chemmater.1c00821
Chem. Mater. 2021, 33, 5021−5034

these defects involved in exsolution and thereby increases the amount of Fe^0 metal formation with higher density and smaller size of particles compared to that on compressively strained films. Our experimental and computational results point to the oxygen vacancy pairs as the nucleation sites for the exsolved nanoparticles on the host oxide. The ability to engineer point defects in exsolution presents pathways for the design of nanostructured catalysts in energy and fuel conversion processes.

METHODS

Film Preparation. The LSF target for pulsed laser deposition (PLD) was synthesized from powders prepared by the shake and bake method. La_2O_3 (Sigma-Aldrich, 99.999%), $SrCO_3$ (Sigma-Aldrich, 99.995%), and Fe_2O_3 (Alfa Aesar, 99.998%) powders were mixed in appropriate ratios and ground using agate mortar and pestle for half an hour and then calcinated at 1000 °C for 5 h with a heating and cooling rate of 5 °C/min. The powders were then pressed into pellets using a hydrostatic press and sintered at 1350 °C for 20 h with a heating and cooling rate of 5 °C/min in stagnant air, thus yielding an LSF target. (001)-oriented 10 × 10 × 0.5 mm^3 single crystal substrates (MTI Corporation, one side polished) were employed in this work. Each crystal substrate was cleaned in methanol (Koptech 200 Proof) in an ultrasonic bath for 3 min before the PLD deposition. The thin-film LSF was deposited with a KrF (λ = 248 nm) excimer laser, at a pulse repetition rate of 5 Hz and a laser energy of 400 mJ. During deposition, the substrate temperature was kept at 650 °C in an oxygen pressure of 20 mTorr. By applying 4000 laser pulses to the LSF target, an LSF thin film of about 20 nm thickness was grown on the substrate (substrate to target distance is 85 mm). After deposition, the sample was cooled in the deposition atmosphere at a cooling rate of 5 °C/min. The as-prepared PLD thin films were not exposed to any further surface treatment to avoid potential contamination. The deposited PLD thin films exhibited desired composition as revealed by ICP measurements (Supplementary Note 8).

Near-Ambient Pressure X-ray Photoelectron Spectroscopy. The NAP-XPS measurements were carried out at the NAP-XPS end station of the Pierre and Marie Curie University set on TEMPO beamline at Synchrotron SOLEIL and the IOS (23-ID-2) beamline of the National Synchrotron Light Source II (NSLS-II) at Brookhaven National Lab. The sample was placed on a ceramic heater, with thermocouples mounted directly onto the surface for temperature measurements. During the measurement, samples were preconditioned at 400 °C in 0.5 mbar O_2 at the beginning of the measurement to remove adventitious carbon, cooled down in UHV, and then gradually heated up to 400 °C in 0.5 mbar flushing H_2 to trigger Fe exsolution. At each temperature, samples were equilibrated for 20 min before the spectra collection.

Atomic Force Microscopy and Reciprocal Space Mapping. *Ex situ* AFM and RSM were performed on the LSF thin films after the NAP-XPS measurement. RSM was collected with a Bruker D8 high-resolution X-ray diffractometer using monochromatic Cu $K\alpha_1$ radiation. To maximize the RSM signal from the film, an asymmetric configuration [103−] is employed for the measurement. AFM images were collected on a Cypher S AFM Microscope with tapping mode, using Bruker TESP-V2 AFM probe. Each of the AFM characterization was done on the center of the sample to avoid edge effects.

Imaging and Elemental Mapping by STEM. The LSF thin film for STEM imaging is grown on 0.5% Nb:STO(001) substrate to enhance sample electronic conductivity. Before characterization, the sample is reduced in 200 sccm 3% H_2/N_2 at 650 °C for 5 h to trigger exsolution. The STEM specimen was prepared by conventional Ga^+ focused ion beam (FIB) lift out procedure using a FIB-SEM (Helios Dual Beam 600). Prior to FIB work, a layer of carbon with 10 nm thickness was deposited on the LSF film by carbon evaporation with EMS QT150 ES. The FIB lamella was thinned using a final Ga ion accelerating voltage of 2 kV with the beam incident at ±1°. The lamella was then polished using 600 eV Ar ions incident at ±10° (Fischione Nanomill). STEM images were acquired using a probe-corrected JEOL ARM 200F operating at 200 kV, and images were calibrated to the substrate Nb:STO(001) lattice spacing of 3.905 nm. Elemental mapping was performed using EDX in the aforementioned STEM.

Surface Defect Modeling. A 100 × 100 2D square lattice with periodic boundary conditions was employed to simulate the oxygen sublattice of the LSF(001) surface (Figure 5b). Since the aim of this simulation is to quantify oxygen vacancy cluster formation, the simulated lattice consists purely of oxygen and oxygen vacancy sites. In the simulated square 2D lattice, the interaction energy between the nearest $V_O^{\bullet\bullet}$ sites was set to be 0.3 eV based on DFT calculation, while all other interactions were ignored. The Metropolis MC simulation was conducted as follows: First, 100 random configurations were generated as initial guesses at each $[V_O^{\bullet\bullet}]$. Then, each of the 100 initial lattices was evolved by switching sites according to the Metropolis scheme. Each MC step consisted of 10 000 switching trials, and the ensemble average was estimated by averaging 500 MCS after equilibrium. Finally, the densities of $V_O^{\bullet\bullet}$-related defects were calculated as the mean value of the 100 thermodynamically equilibrated lattices. In accord with the experiment, the simulation temperature was set to be 650 °C and the lattice constant for the 2D lattice was set to be 0.4 nm. A more detailed description of the MC simulation procedure is presented in ref 72.

Density Functional Theory. DFT calculations are performed with the Vienna *ab initio* Simulation Package (VASP) with PAW-PW91 pseudopotentials. Energy cut-off is set to 500 eV. A Hubbard U correction of 4.0 eV is applied to Fe. All calculations are spin-polarized. Defect formation energies in the bulk are calculated using a 2 × 2 × 2 $La_{0.5}Sr_{0.5}FeO_3$ supercell (8 formula units) with the ordered alternating layers of La and Sr.[73] A 4 × 4 × 4 *k*-point grid is used. Multiple vacancy sites are considered and the configurations with the lowest energies are reported. Fe dimer formation calculations are performed on a 2 × 2 BO-terminated LSF surface with 10 atomic layers (40 formula units) and 20 Å of vacuum. The five atomic layers in the middle are fixed during the structural relaxation to mimic bulk LSF. A 2 × 2 × 1 *k*-point grid is used. The atomic structures used in the DFT calculation are presented in Supplementary Note 7.

ASSOCIATED CONTENT

Supporting Information

The Supporting Information is available free of charge at https://pubs.acs.org/doi/10.1021/acs.chemmater.1c00821.

Details of the experimental and computational procedure, thermodynamic analysis of the exsolution condition, defect chemistry and diffusion characteristics of LSF, quantification of lattice strain, XPS and AFM analysis, and additional physical and chemical characterization (PDF)

AUTHOR INFORMATION

Corresponding Author

Bilge Yildiz − *Department of Nuclear Science and Engineering and Department of Materials Science and Engineering, Massachusetts Institute of Technology, Cambridge, Massachusetts 02139, United States;* orcid.org/0000-0002-2688-5666; Email: byildiz@mit.edu

Authors

Jiayue Wang − *Department of Nuclear Science and Engineering, Massachusetts Institute of Technology, Cambridge, Massachusetts 02139, United States;* orcid.org/0000-0002-2027-3634

Jing Yang − *Department of Materials Science and Engineering, Massachusetts Institute of Technology, Cambridge,*

Massachusetts 02139, United States; orcid.org/0000-0003-1855-0708

Alexander K. Opitz − *Department of Nuclear Science and Engineering, Massachusetts Institute of Technology, Cambridge, Massachusetts 02139, United States; Institute of Chemical Technologies and Analytics, TU Wien, 1060 Vienna, Austria;* orcid.org/0000-0002-2567-1885

William Bowman − *Department of Nuclear Science and Engineering, Massachusetts Institute of Technology, Cambridge, Massachusetts 02139, United States;* orcid.org/0000-0002-4346-1144

Roland Bliem − *Department of Nuclear Science and Engineering, Massachusetts Institute of Technology, Cambridge, Massachusetts 02139, United States;* orcid.org/0000-0002-8714-8942

Georgios Dimitrakopoulos − *Department of Nuclear Science and Engineering, Massachusetts Institute of Technology, Cambridge, Massachusetts 02139, United States; Department of Mechanical Engineering, Massachusetts Institute of Technology, Cambridge, Massachusetts 02139, United States;* orcid.org/0000-0001-6636-0517

Andreas Nenning − *Institute of Chemical Technologies and Analytics, TU Wien, 1060 Vienna, Austria*

Iradwikanari Waluyo − *National Synchrotron Light Source II, Brookhaven National Laboratory, Upton, New York 11973, United States;* orcid.org/0000-0002-4046-9722

Adrian Hunt − *National Synchrotron Light Source II, Brookhaven National Laboratory, Upton, New York 11973, United States*

Jean-Jacques Gallet − *Laboratoire de Chimie Physique Matière et Rayonnement − Campus Pierre et Marie Curie, Sorbonne Université, CNRS, F-75005 Paris, France; Synchrotron SOLEIL, L'Orme des Merisiers, Saint-Aubin F-91192, Gif-sur-Yvette, France*

Complete contact information is available at: https://pubs.acs.org/10.1021/acs.chemmater.1c00821

Author Contributions

J.W., A.K.O., and B.Y. conceived the experiment design. J.W. prepared and characterized the samples. J.W., A.K.O, R.B., G.D., A.N., I.W., A.H., and J.-J.G. carried out the NAP-XPS experiments. J.Y. performed the DFT calculations and J.W. performed the MC simulations. W.B. conducted the STEM imaging. J.W. and B.Y. wrote the manuscript and all authors contributed to its revision. B.Y. supervised the project.

Notes

The authors declare no competing financial interest.

■ ACKNOWLEDGMENTS

The authors are grateful to the Exelon Corporation for the funding support. This research used the synchrotron radiation facilities at the National Synchrotron Light Source II (23-ID-2/IOS beamline), a U.S. Department of Energy (DOE) Office of Science User Facility operated for the DOE Office of Science by Brookhaven National Laboratory under contract no. DE-SC0012704, and the TEMPO beamline at the Synchrotron SOLEIL. This work was performed in part at the Center for Nanoscale Systems (CNS) at Harvard University, a member of the National Nanotechnology Coordinated Infrastructure Network (NNCI), which was supported by the National Science Foundation under NSF award no. 1541959. The authors acknowledge the facility support from the Center for Materials Science and Engineering (NSF under award no. DMR-1419807) at MIT. The authors also thank the Photoemission End Stations (BL10B) in National Synchrotron Radiation Laboratory (NSRL) for the preliminary characterizations. J.W. and A.K.O. thank Christopher Herzig (TU Wien) for the assistance in the ICP measurements.

■ REFERENCES

(1) Munnik, P.; De Jongh, P. E.; De Jong, K. P. Recent Developments in the Synthesis of Supported Catalysts. *Chem. Rev.* **2015**, *115*, 6687−6718.

(2) Liu, L.; Corma, A. Metal Catalysts for Heterogeneous Catalysis: From Single Atoms to Nanoclusters and Nanoparticles. *Chem. Rev.* **2018**, *118*, 4981−5079.

(3) Van Deelen, T. W.; Hernández Mejía, C.; De Jong, K. P. Control of metal-support interactions in heterogeneous catalysts to enhance activity and selectivity. *Nat. Catal.* **2019**, *2*, 955−970.

(4) Nishihata, Y.; Mizuki, J.; Akao, T.; Tanaka, H.; Uenishi, M.; Kimura, M.; Okamoto, T.; Hamada, N. Self-regeneration of a Pd-perovskite catalyst for automotive emissions control. *Nature* **2002**, *418*, 164−167.

(5) Seshadri, R. Oxide Nanoparticles. *Chem. Nanomater.* **2004**, 94−112.

(6) Neagu, D.; Oh, T.-S.; Miller, D. N.; Ménard, H.; Bukhari, S. M.; Gamble, S. R.; Gorte, R. J.; Vohs, J. M.; Irvine, J. T. S. Nano-socketed nickel particles with enhanced coking resistance grown in situ by redox exsolution. *Nat. Commun.* **2015**, *6*, No. 8120.

(7) Neagu, D.; Papaioannou, E. I.; Ramli, W. K. W.; Miller, D. N.; Murdoch, B. J.; Ménard, H.; Umar, A.; Barlow, A. J.; Cumpson, P. J.; Irvine, J. T. S.; Metcalfe, I. S. Demonstration of chemistry at a point through restructuring and catalytic activation at anchored nanoparticles. *Nat. Commun.* **2017**, *8*, No. 1855.

(8) Jo, Y.-R.; Koo, B.; Seo, M. J.; Kim, J. K.; Lee, S.; Kim, K.; Han, J. W.; Jung, W.; Kim, B. J. Growth Kinetics of Individual Co Particles Ex-solved on $SrTi_{0.75}Co_{0.25}O_{3-\delta}$ Polycrystalline Perovskite Thin Films. *J. Am. Chem. Soc.* **2019**, *141*, 6690−6697.

(9) Neagu, D.; Kyriakou, V.; Roiban, I.-L.; Aouine, M.; Tang, C.; Caravaca, A.; Kousi, K.; Schreur-Piet, I.; Metcalfe, I. S.; Vernoux, P.; Van De Sanden, M. C. M.; Tsampas, M. N. In Situ Observation of Nanoparticle Exsolution from Perovskite Oxides: From Atomic Scale Mechanistic Insight to Nanostructure Tailoring. *ACS Nano* **2019**, *13*, 12996−13005.

(10) Dai, S.; Zhang, S.; Katz, M. B.; Graham, G. W.; Pan, X. In Situ Observation of Rh-$CaTiO_3$ Catalysts during Reduction and Oxidation Treatments by Transmission Electron Microscopy. *ACS Catal.* **2017**, *7*, 1579−1582.

(11) Lai, K.-Y.; Manthiram, A. Evolution of Exsolved Nanoparticles on a Perovskite Oxide Surface during a Redox Process. *Chem. Mater.* **2018**, *30*, 2838−2847.

(12) Gao, Z.; Mogni, L. V.; Miller, E. C.; Railsback, J. G.; Barnett, S. A. A perspective on low-temperature solid oxide fuel cells. *Energy Environ. Sci.* **2016**, *9*, 1602−1644.

(13) Zhu, T.; Troiani, H. E.; Mogni, L. V.; Han, M.; Barnett, S. A. Ni-Substituted $Sr(Ti,Fe)O_3$ SOFC Anodes: Achieving High Performance via Metal Alloy Nanoparticle Exsolution. *Joule* **2018**, *2*, 478−496.

(14) Myung, J.-H.; Neagu, D.; Miller, D. N.; Irvine, J. T. S. Switching on electrocatalytic activity in solid oxide cells. *Nature* **2016**, *537*, 528−531.

(15) Wu, X.-Y.; Ghoniem, A. F. Mixed ionic-electronic conducting (MIEC) membranes for thermochemical reduction of CO_2: A review. *Prog. Energy Combust. Sci.* **2019**, *74*, 1−30.

(16) Dimitrakopoulos, G.; Ghoniem, A. F.; Yildiz, B. In situ catalyst exsolution on perovskite oxides for the production of CO and synthesis gas in ceramic membrane reactors. *Sustainable Energy Fuels* **2019**, *3*, 2347−2355.

(17) Kousi, K.; Neagu, D.; Bekris, L.; Papaioannou, E. I.; Metcalfe, I. S. Endogenous Nanoparticles Strain Perovskite Host Lattice Providing Oxygen Capacity and Driving Oxygen Exchange and CH_4 Conversion to Syngas. *Angew. Chem., Int. Ed.* **2020**, *59*, 2510−2519.
(18) Sun, Y.-F.; Yang, Y.-L.; Chen, J.; Li, M.; Zhang, Y.-Q.; Li, J.-H.; Hua, B.; Luo, J.-L. Toward a rational photocatalyst design: A new formation strategy of co-catalyst/semiconductor heterostructures via in situ exsolution. *Chem. Commun.* **2018**, *54*, 1505−1508.
(19) Haruta, M. Size- and support-dependency in the catalysis of gold. *Catal. Today* **1997**, *36*, 153−166.
(20) Kobsiriphat, W.; Madsen, B. D.; Wang, Y.; Shah, M.; Marks, L. D.; Barnett, S. A. Nickel- and Ruthenium-Doped Lanthanum Chromite Anodes: Effects of Nanoscale Metal Precipitation on Solid Oxide Fuel Cell Performance. *J. Electrochem. Soc.* **2010**, *157*, B279−B284.
(21) Wang, Y.; Liu, T.; Li, M.; Xia, C.; Zhou, B.; Chen, F. Exsolved Fe−Ni nano-particles from $Sr_2Fe_{1.3}Ni_{0.2}$ $Mo_{0.5}O_6$ perovskite oxide as a cathode for solid oxide steam electrolysis cells. *J. Mater. Chem. A* **2016**, *4*, 14163−14169.
(22) Götsch, T.; Köpfle, N.; Grünbacher, M.; Bernardi, J.; Carbonio, E. A.; Hävecker, M.; Knop-Gericke, A.; Bekheet, M. F.; Schlicker, L.; Doran, A.; Gurlo, A.; Franz, A.; Klötzera, B.; Penner, S. Crystallographic and electronic evolution of lanthanum strontium ferrite ($La_{0.6}Sr_{0.4}FeO_{3-\delta}$) thin film and bulk model systems during iron exsolution. *Phys. Chem. Chem. Phys.* **2019**, *21*, 3781−3794.
(23) Kwon, O.; Sengodan, S.; Kim, K.; Kim, G.; Jeong, H. Y.; Shin, J.; Ju, Y.-W.; Han, J. W.; Kim, G. Exsolution trends and co-segregation aspects of self-grown catalyst nanoparticles in perovskites. *Nat. Commun.* **2017**, *8*, No. 15967.
(24) Raman, A. S.; Vojvodic, A. Modeling Exsolution of Pt from ATiO 3Perovskites (A = Ca/Sr/Ba) Using First-Principles Methods. *Chem. Mater.* **2020**, *32*, 9642−9649.
(25) Neagu, D.; Tsekouras, G.; Miller, D. N.; Ménard, H.; Irvine, J. T. S. In situ growth of nanoparticles through control of non-stoichiometry. *Nat. Chem.* **2013**, *5*, 916−923.
(26) Sun, Y.-F.; Zhang, Y.-Q.; Chen, J.; Li, J.-H.; Zhu, Y.-T.; Zeng, Y.-M.; Amirkhiz, B. S.; Li, J.; Hua, B.; Luo, J.-L. New Opportunity for in Situ Exsolution of Metallic Nanoparticles on Perovskite Parent. *Nano Lett.* **2016**, *16*, 5303−5309.
(27) Bäumer, M.; Frank, M.; Heemeier, M.; Kühnemuth, R.; Stempel, S.; Freund, H.-J. Nucleation and growth of transition metals on a thin alumina film. *Surf. Sci.* **2000**, *454*−*456*, 957−962.
(28) Haas, G.; Menck, A.; Brune, H.; Barth, J. V.; Venables, J. A.; Kern, K. Nucleation and growth of supported clusters at defect sites: Pd/MgO(001). *Phys. Rev. B* **2000**, *61*, 11105−11108.
(29) Thanh, N. T. K.; Maclean, N.; Mahiddine, S. Mechanisms of Nucleation and Growth of Nanoparticles in Solution. *Chem. Rev.* **2014**, *114*, 7610−7630.
(30) Yanagisawa, S.; Uozumi, A.; Hamada, I.; Morikawa, Y. Search for a Self-Regenerating Perovskite Catalyst Using Ab Initio Thermodynamics Calculations. *J. Phys. Chem. C* **2013**, *117*, 1278−1286.
(31) Tanaka, H.; Taniguchi, M.; Uenishi, M.; Kajita, N.; Tan, I.; Nishihata, Y.; Mizuki, J.; Narita, K.; Kimura, M.; Kaneko, K. Self-Regenerating Rh- and Pt-Based Perovskite Catalysts for Automotive-Emissions Control. *Angew. Chem., Int. Ed.* **2006**, *45*, 5998−6002.
(32) Hamada, I.; Uozumi, A.; Morikawa, Y.; Yanase, A.; Katayama-Yoshida, H. A Density Functional Theory Study of Self-Regenerating Catalysts $LaFe_{1-x}M_xO_{3-y}$ (M = Pd, Rh, Pt). *J. Am. Chem. Soc.* **2011**, *133*, 18506−18509.
(33) Tian, Z.; Uozumi, A.; Hamada, I.; Yanagisawa, S.; Kizaki, H.; Inagaki, K.; Morikawa, Y. First-principles investigation on the segregation of Pd at $LaFe_{1-x}Pd_xO_{3-y}$ surfaces. *Nanoscale Res. Lett.* **2013**, *8*, 1−7.
(34) Gao, Y.; Lu, Z.; You, T. L.; Wang, J.; Xie, L.; He, J.; Ciucci, F. Energetics of Nanoparticle Exsolution from Perovskite Oxides. *J. Phys. Chem. Lett.* **2018**, *9*, 3772−3778.
(35) Kushima, A.; Yip, S.; Yildiz, B. Competing strain effects in reactivity of $LaCoO_3$ with oxygen. *Phys. Rev. B* **2010**, *82*, No. 115435.
(36) Aschauer, U.; Pfenninger, R.; Selbach, S. M.; Grande, T.; Spaldin, N. A. Strain-controlled oxygen vacancy formation and ordering in $CaMnO_3$. *Phys. Rev. B* **2013**, *88*, No. 054111.
(37) Kushima, A.; Yildiz, B. Oxygen ion diffusivity in strained yttria stabilized zirconia: Where is the fastest strain? *J. Mater. Chem.* **2010**, *20*, 4809−4819.
(38) Gazquez, J.; Bose, S.; Sharma, M.; Torija, M. A.; Pennycook, S. J.; Leighton, C.; Varela, M. Lattice mismatch accommodation via oxygen vacancy ordering in epitaxial $La_{0.5}Sr_{0.5}CoO_{3-\delta}$ thin films. *APL Mater.* **2013**, *1*, No. 012105.
(39) Orikasa, Y.; Nakao, T.; Oishi, M.; Ina, T.; Mineshige, A.; Amezawa, K.; Arai, H.; Ogumi, Z.; Uchimoto, Y. Local structural analysis for oxide ion transport in $La_{0.6}Sr_{0.4}FeO_{3-\delta}$ cathodes. *J. Mater. Chem.* **2011**, *21*, 14013−14019.
(40) Kuhn, M.; Hashimoto, S.; Sato, K.; Yashiro, K.; Mizusaki, J. Oxygen nonstoichiometry, thermo-chemical stability and lattice expansion of $La_{0.6}Sr_{0.4}FeO_{3-\delta}$. *Solid State Ionics* **2011**, *195*, 7−15.
(41) Thalinger, R.; Gocyla, M.; Heggen, M.; Klötzer, B.; Penner, S. Exsolution of Fe and SrO Nanorods and Nanoparticles from Lanthanum Strontium Ferrite $La_{0.6}Sr_{0.4}FeO_{3-\delta}$ Materials by Hydrogen Reduction. *J. Phys. Chem. C* **2015**, *119*, 22050−22056.
(42) Nenning, A.; Fleig, J. Electrochemical XPS investigation of metal exsolution on SOFC electrodes: Controlling the electrode oxygen partial pressure in ultra-high-vacuum. *Surf. Sci.* **2019**, *680*, 43−51.
(43) Opitz, A. K.; Nenning, A.; Rameshan, C.; Rameshan, R.; Blume, R.; Hävecker, M.; Knop-Gericke, A.; Rupprechter, G.; Fleig, J.; Klötzer, B. Enhancing Electrochemical Water-Splitting Kinetics by Polarization-Driven Formation of Near-Surface Iron(0): An In Situ XPS Study on Perovskite-Type Electrodes. *Angew. Chem., Int. Ed.* **2014**, *127*, 2666−2670.
(44) Opitz, A. K.; Nenning, A.; Vonk, V.; Volkov, S.; Bertram, F.; summerer, H.; Schwarz, S.; Steiger-Thirsfeld, A.; Bernardi, J.; Stierle, A.; Fleig, J. Understanding electrochemical switchability of perovskite-type exsolution catalysts. *Nat. Commun.* **2020**, *11*, No. 4801.
(45) Katz, M. B.; Graham, G. W.; Duan, Y.; Liu, H.; Adamo, C.; Schlom, D. G.; Pan, X. Self-Regeneration of Pd−aFeO_3 Catalysts: New Insight from Atomic-Resolution Electron Microscopy. *J. Am. Chem. Soc.* **2011**, *133*, 18090−18093.
(46) Katz, M. B.; Zhang, S.; Duan, Y.; Wang, H.; Fang, M.; Zhang, K.; Li, B.; Graham, G. W.; Pan, X. Reversible precipitation/dissolution of precious-metal clusters in perovskite-based catalyst materials: Bulk versus surface re-dispersion. *J Catal.* **2012**, *293*, 145−148.
(47) Kim, K.; Koo, B.; Jo, Y. R.; Lee, S.; Kim, J. K.; Kim, B. J.; Jung, W.; Han, J. W. Control of transition metal−oxygen bond strength boosts the redox ex-solution in a perovskite oxide surface. *Energy Environ. Sci.* **2020**, *13*, 3404−3411.
(48) Han, H.; Park, J.; Nam, S. Y.; Kim, K. J.; Choi, G. M.; Parkin, S. S. P.; Jang, H. M.; Irvine, J. T. S. Lattice strain-enhanced exsolution of nanoparticles in thin films. *Nat. Commun.* **2019**, *10*, No. 1471.
(49) Gopal, C. B.; Gabaly, F. E.; McDaniel, A. H.; Chueh, W. C. Origin and Tunability of Unusually Large Surface Capacitance in Doped Cerium Oxide Studied by Ambient-Pressure X-Ray Photoelectron Spectroscopy. *Adv. Mater.* **2016**, *28*, 4692−4697.
(50) Crumlin, E. J.; Mutoro, E.; Liu, Z.; Grass, M. E.; Biegalski, M. D.; Lee, Y.-L.; Morgan, D.; Christen, H. M.; Bluhm, H.; Shao-Horn, Y. Surface strontium enrichment on highly active perovskites for oxygen electrocatalysis in solid oxide fuel cells. *Energy Environ. Sci.* **2012**, *5*, 6081−6088.
(51) Opitz, A. K.; Rameshan, C.; Kubicek, M.; Rupp, G. M.; Nenning, A.; Götsch, T.; Blume, R.; Hävecker, M.; Knop-Gericke, A.; Rupprechter, G.; Klötzer, B.; Fleig, J. The Chemical Evolution of the $La_{0.6}Sr_{0.4}CoO_{3-\delta}$ Surface Under SOFC Operating Conditions and Its Implications for Electrochemical Oxygen Exchange Activity. *Top. Catal.* **2018**, *61*, 2129−2141.
(52) Tuller, H. L.; Bishop, S. R. Point Defects in Oxides: Tailoring Materials Through Defect Engineering. *Annu. Rev. Mater. Res.* **2011**, *41*, 369−398.

https://doi.org/10.1021/acs.chemmater.1c00821
Chem. Mater. 2021, 33, 5021−5034

(53) Marrocchelli, D.; Bishop, S. R.; Tuller, H. L.; Yildiz, B. Understanding Chemical Expansion in Non-Stoichiometric Oxides: Ceria and Zirconia Case Studies. *Adv. Funct. Mater.* **2012**, *22*, 1958−1965.
(54) Götsch, T.; Schlicker, L.; Bekheet, M. F.; Doran, A.; Grünbacher, M.; Praty, C.; Tada, M.; Matsui, H.; Ishiguro, N.; Gurlo, A.; Klötzera, B.; Penner, S. Structural investigations of $La_{0.6}Sr_{0.4}FeO_{3-\delta}$ under reducing conditions: Kinetic and thermodynamic limitations for phase transformations and iron exsolution phenomena. *RSC Adv.* **2018**, *8*, 3120−3131.
(55) Mueller, D. N.; Machala, M. L.; Bluhm, H.; Chueh, W. C. Redox activity of surface oxygen anions in oxygen-deficient perovskite oxides during electrochemical reactions. *Nat. Commun.* **2015**, *6*, No. 6097.
(56) Aschauer, U.; Vonrüti, N.; Spaldin, N. A. Effect of epitaxial strain on cation and anion vacancy formation in MnO. *Phys. Rev. B* **2015**, *92*, No. 054103.
(57) Xia, L.; Tybell, T.; Selbach, S. M. Bi vacancy formation in BiFeO 3epitaxial thin films under compressive (001)-strain from first principles. *J. Mater. Chem. C* **2019**, *7*, 4870−4878.
(58) Zhang, B.; Fan, M.; Li, L.; Jian, J.; Huang, J.; Wang, H.; Kalaswad, M.; Wang, H. Tunable magnetic anisotropy of self-assembled Fe nanostructures within a $La_{0.5}Sr_{0.5}$ FeO_3 matrix. *Appl. Phys. Lett.* **2018**, *112*, No. 013104.
(59) Mohaddes-Ardabili, L.; Zheng, H.; Ogale, S. B.; Hannoyer, B.; Tian, W.; Wang, J.; Lofland, S. E.; Shinde, S. R.; Zhao, T.; Jia, Y.; Salamanca-Riba, L.; Schlom, D. G.; Wuttig, M.; Ramesh, R. Self-assembled single-crystal ferromagnetic iron nanowires formed by decomposition. *Nat. Mater.* **2004**, *3*, 533−538.
(60) Götsch, T.; Köpfle, N.; Schlicker, L.; Carbonio, E. A.; Hävecker, M.; Knop-Gericke, A.; Schloegl, R.; Bekheet, M. F.; Gurlo, A.; Doran, A. Treading in the Limited Stability Regime of Lanthanum Strontium Ferrite—Reduction, Phase Change and Exsolution. *ECS Trans.* **2019**, *91*, 1771−1781.
(61) Shen, J.; Zhang, D.; Zhang, F.-H.; Gan, Y. AFM tip-sample convolution effects for cylinder protrusions. *Appl. Surf. Sci.* **2017**, *422*, 482−491.
(62) Gan, Y. Atomic and subnanometer resolution in ambient conditions by atomic force microscopy. *Surf. Sci. Rep.* **2009**, *64*, 99−121.
(63) Opitz, A. K.; Nenning, A.; Kogler, S.; Rameshan, C.; Rameshan, R.; Blume, R.; Haevecker, M.; Knop-Gericke, A.; Rupprechter, G.; Kloetzer, B. Water Splitting on Model-Composite $La_{0.6}Sr_{0.4}FeO_{3-\delta}$ (LSF) Electrodes in H_2/H_2O Atmosphere. *ECS Trans.* **2015**, *68*, 3333−3343.
(64) Flytzani-Stephanopoulos, M.; Gates, B. C. Atomically Dispersed Supported Metal Catalysts. *Annu. Rev. Chem. Biomol. Eng.* **2012**, *3*, 545−574.
(65) Kim, K. J.; Han, H.; Defferriere, T.; Yoon, D.; Na, S.; Kim, S. J.; Dayaghi, A. M.; Son, J.; Oh, T.-S.; Jang, H. M.; Choi, G. M. Facet-Dependent In Situ Growth of Nanoparticles in Epitaxial Thin Films: The Role of Interfacial Energy. *J. Am. Chem. Soc.* **2019**, *141*, 7509−7517.
(66) Min, B. K.; Wallace, W. T.; Santra, A. K.; Goodman, D. W. Role of Defects in the Nucleation and Growth of Au Nanoclusters on SiO_2 Thin Films. *J. Phys. Chem. B* **2004**, *108*, 16339−16343.
(67) Wahlström, E.; Lopez, N.; Schaub, R.; Thostrup, P.; Rønnau, A.; Africh, C.; Lægsgaard, E.; Nørskov, J. K.; Besenbacher, F. Bonding of Gold Nanoclusters to Oxygen Vacancies on Rutile TiO_2(110). *Phys. Rev. Lett.* **2003**, *90*, No. 026101.
(68) Zhang, C.; Michaelides, A.; King, D. A.; Jenkins, S. J. Anchoring Sites for Initial Au Nucleation on CeO 2{111}: O Vacancy versus Ce Vacancy. *J. Phys. Chem. C* **2009**, *113*, 6411−6417.
(69) Giordano, L.; Di Valentin, C.; Goniakowski, J.; Pacchioni, G. Nucleation of Pd Dimers at Defect Sites of the MgO(100) Surface. *Phys. Rev. Lett.* **2004**, *92*, No. 096105.
(70) Kwak, N. W.; Jeong, S. J.; Seo, H. G.; Lee, S.; Kim, Y.; Kim, J. K.; Byeon, P.; Chung, S.-Y.; Jung, W. In situ synthesis of supported metal nanocatalysts through heterogeneous doping. *Nat. Commun.* **2018**, *9*, No. 4829.
(71) Cahn, J. W. The kinetics of grain boundary nucleated reactions. *Acta Metall.* **1956**, *4*, 449−459.
(72) Wang, J.; Bishop, S. R.; Sun, L.; Lu, Q.; Vardar, G.; Bliem, R.; Tsvetkov, N.; Crumlin, E. J.; Gallet, J.-J.; Bournel, F.; Waluyo, I.; Yildiz, B. Threshold catalytic onset of carbon formation on CeO_2 during CO_2 electrolysis: Mechanism and inhibition. *J. Mater. Chem. A* **2019**, *7*, 15233−15243.
(73) Maiti, D.; Daza, Y. A.; Yung, M. M.; Kuhn, J. N.; Bhethanabotla, V. R. Oxygen vacancy formation characteristics in the bulk and across different surface terminations of $La_{(1-x)}Sr_xFe_{(1-y)}Co_yO_{(3-\delta)}$ perovskite oxides for CO_2 conversion. *J. Mater. Chem. A* **2016**, *4*, 5137−5148.

https://doi.org/10.1021/acs.chemmater.1c00821
Chem. Mater. 2021, 33, 5021−5034

Supporting Information

Tuning point defects by elastic strain modulates nanoparticle exsolution on perovskite oxides

Jiayue Wang[1], Jing Yang[2], Alexander K. Opitz[1,3], William Bowman[1], Roland Bliem[1#], Georgios Dimitrakopoulos[1,4], Andreas Nenning[3], Iradwikanari Waluyo[5], Adrian Hunt[5], Jean-Jacques Gallet[6,7], Bilge Yildiz[1,2]*

[1]Department of Nuclear Science and Engineering, Massachusetts Institute of Technology, Cambridge, Massachusetts 02139, USA

[2]Department of Materials Science and Engineering, Massachusetts Institute of Technology, Cambridge, Massachusetts 02139, USA

[3]Institute of Chemical Technologies and Analytics, TU Wien, 1060 Vienna, Austria

[4]Department of Mechanical Engineering, Massachusetts Institute of Technology, Cambridge, Massachusetts 02139, USA

[5]National Synchrotron Light Source II, Brookhaven National Laboratory, Upton, New York 11973, USA

[6]Sorbonne Université, CNRS, Laboratoire de Chimie Physique Matière et Rayonnement – Campus Pierre et Marie Curie, F-75005 Paris, France

[7]Synchrotron SOLEIL, L'Orme des Merisiers, Saint-Aubin, F-91192 Gif-sur-Yvette, France

* e-mail: byildiz@mit.edu

#: Present affiliation, Advanced Research Center for Nanolithography, Science Park 106, 1098XG Amsterdam, The Netherlands, and Institute of Physics, University of Amsterdam, Science Park 904, 1098XH, Amsterdam, The Netherlands

Supplementary Note 1: Quantification of effective pO_2 at the exsolution condition

It has been reported that the change of defect chemistry under different oxygen partial pressures (pO_2) can induce a shift in the binding energy. In particular, in LSF, the binding energy shift (Δ B.E.) is related to the different chemical potentials of oxygen in the two atmospheres ($\Delta \mu_{O_2}$)[1,2]:

$$\Delta \text{ B.E.} = -e \times \frac{\Delta \mu_{O_2}}{4F} = e \times \frac{RT}{4F} \ln \frac{pO_2}{pO_2^{\text{eff}}}$$

where *R* and *F* represent the gas constant and Faraday constant, respectively. As a result, by measuring the binding energy shift, we can estimate the effective pO_2 at the exsolution condition (400 °C in 0.5 mbar H_2).

As shown in **Figure S1**, the binding energies of Sr 3*d*, La 4*d*, and Fe 3*p* increased by about 1.1 eV when the gas atmosphere was changed from 0.5 mbar O_2 to 0.5 mbar H_2. Therefore, we can estimate the effective pO_2 to be 4×10^{-38} bar for the flushing H_2 environment in Figure 1a. A more detailed procedure on the effective pO_2 calculation can be found in Ref. [1,2].

With the calculated effective pO_2, we can also verify the oxidation states of the exsolved Fe^0 nanoparticles using Richardson–Ellingham diagram. This diagram shows the most stable formula of substances in terms of their redox equilibria. The equilibria for Fe, Fe_3O_4, and Fe_2O_3 are shown in **Figure S2**. As illustrated, for the exsolution condition in this experiment (400 °C, 4×10^{-38} pO_2), the most stable phase is indeed metallic iron.

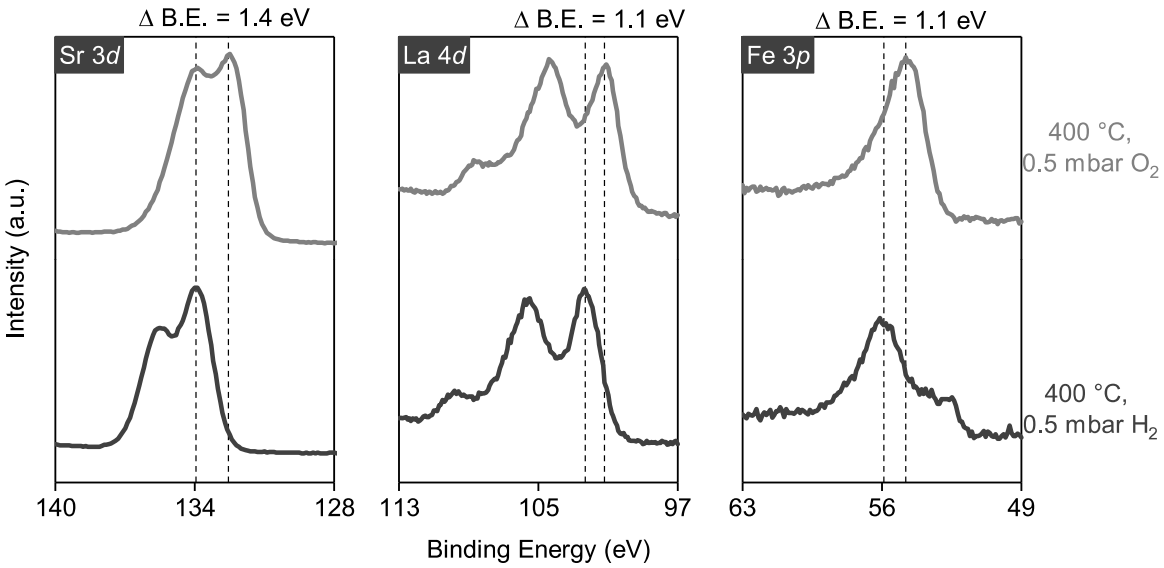

Figure S1. Core level peak shift between 0.5 mbar of O_2 and H_2 at 400 °C, which is largely caused by the Fermi level shift. Assume all the 1.1 eV peak shift is due to Fermi level shift, we can estimate that the equivalent pO_2 to be 4×10^{-38} bar for the reducing atmosphere. Data were collected on LSF/STO with a photon energy of 420 eV.

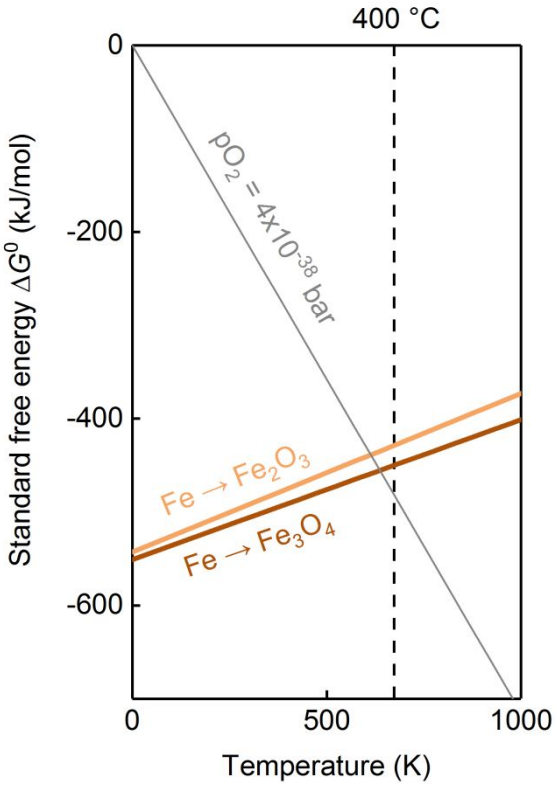

Figure S2. Richardson–Ellingham diagram for the Fe–O system. The standard Gibbs energies reflect the formation of oxides per one mole of oxygen gas. Note at the exsolution condition, the most stable phase is metallic iron.

Supplementary Note 2: Quantification of [Fe^0]

The low binding energy component in Fe 3*p* at ~ 51.5 eV was assigned to Fe^0 species[3]. [Fe^0] was thus calculated as the peak area ratio of Fe^0 features to the total area of Fe 3*p* with CasaXPS software. The peak area ratio is calculated through peak fitting, where peaks were fitted with a 30% Lorentz/Gaussian line shape over a Shirley background. The uncertainties in the peak fitting process is estimated to be ~2%, based on the standard deviation of the [Fe^0] calculated from Fe 3*p* and Fe 2*p* spectra.

To verify the peak assignment of Fe^0, we also performed lab-based XPS on Fe (Aldrich, 99.99%), FeO (Aldrich, 99.8%), and Fe_2O_3 (Alfa Aesar, 99.998%) powders and the corresponding Fe 2*p* and Fe 3*p* spectra are shown in **Figure S3**. As can be seen, the as-received Fe powders are partially oxidized in the near surface region, hence containing both metallic and oxidized iron components in the XPS spectra. A pure Fe^0 XPS spectrum is then obtained on a Fe foil (Aldrich, 99.9%) after sputtering the sample with 2 keV Ar^+ ions for 5 minutes. The metallic peak position observed in this measurement is in accord with the emerging feature during Fe exsolution, which validates our previous assignment of this feature as Fe^0.

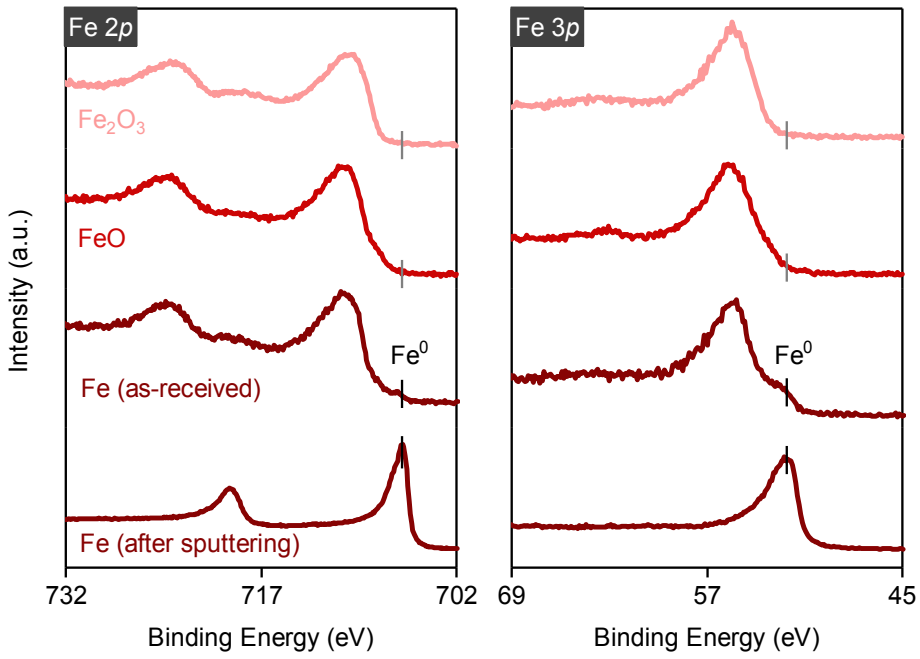

Figure S3. Reference Fe 2*p* and 3*p* XPS spectra of Fe_2O_3, FeO, and Fe, where the Fe^0 peak position is highlighted in the plot. Note the as-received Fe powder has FeO_x components in the spectra as its surface is partially oxidized. Pure Fe^0 spectra is then collected on a Fe foil after Ar ion sputtering. The spectra are collected with lab-based XPS and then calibrated by aligning the adventitious C 1s spectra at 284.8 eV.

Supplementary Note 3: Quantification of oxygen nonstoichiometry in LSF

A schematic diagram of the oxygen non-stoichiometry of LSF as a function of oxygen partial pressure at a given temperature is shown in **Figure S4**. As can be seen, there are three regions in this diagram: the O^-/O^{2-} redox region[4] where the Sr doping is charge compensated by electron holes (Region I); the plateau region where the oxygen vacancy concentration is almost constant as it is determined by the Sr doping level (Region II); and the Fe^{3+}/Fe^{2+} redox region where additional oxygen vacancy formation is charge compensated by the electrons (Region III). Note that at very reducing atmospheres in Region III, the LSF perovskite phase becomes unstable and starts to decompose when $\delta > 0.25$. This critical oxygen nonstoichiometry corresponds to a nominal bulk oxygen vacancy concentration of $\sim 8\%$.

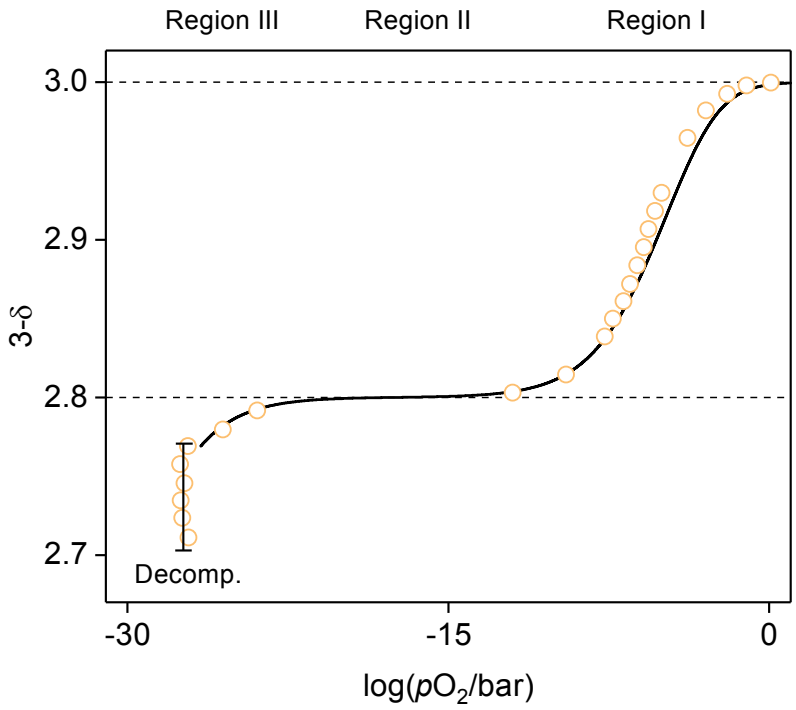

Figure S4. Oxygen non-stoichiometry of $La_{0.6}Sr_{0.4}FeO_{3-\delta}$ as a function of oxygen partial pressure at 600 °C, data replotted from Ref. [5].

In this work, we used XPS and XRD to quantify the oxygen nonstoichiometry change ($\Delta\delta$) in LSF. For XPS, $\Delta\delta$ was calculated from the normalized O 1*s* peak intensity, as has been reported elsewhere[6]. To specify, the O 1*s* spectra are first normalized to the La 4*d* signal intensity to avoid fluctuations caused by slight variations in beam intensity and by effects owing to sample heating and gas atmosphere[7]. Then the change in surface oxygen nonstoichiometry relative to the oxidized surface is calculated as follows:

$$\Delta\delta = 1 - \frac{A(O_{1s})}{A(O_{1s})_{\text{oxidized}}}$$

where A denotes the peak area of the normalized O $1s$ spectra, and the subscript "oxidized" denotes the spectra collected on an oxidized sample surface (400 °C, 0.5 mbar O_2). As shown in **Figure S5**, the oxidized reference surface is free of carbon, which eliminates the potential contribution from carbonate oxygen species.

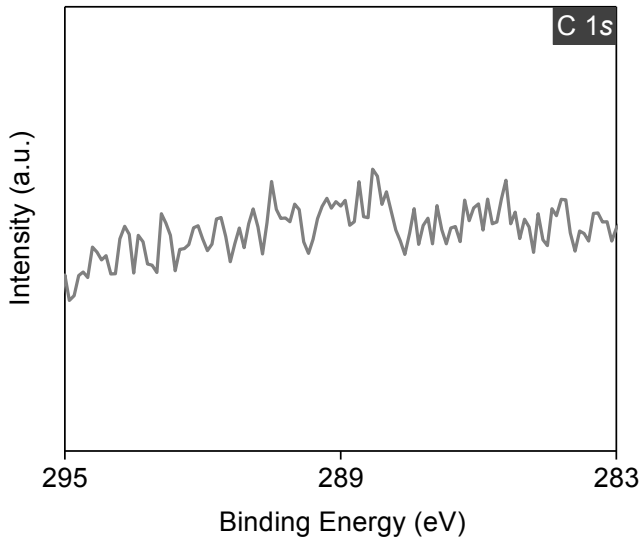

Figure S5. Typical C $1s$ spectra of the oxidized LSF surface. Spectrum was collected on LSF/STO, at 400 °C in 0.5 mbar O_2 with a photon energy of 420 eV.

It should be noted that, due to the lack of an internal normalization procedure for the O $1s$, this method is only semi-quantitative. Therefore, we only employed this method to analyze the O $1s$ spectra collected from LSF/STO in a single experiment. Since the purpose is to qualitatively demonstrate the evolution of oxygen nonstoichiometry during Fe exsolution, rather than to precisely calculate [$V_O^{\bullet\bullet}$], the possible uncertainties in the method should not be a major problem. In this work, the error bar was estimated based on the square root of the calculated $\Delta\delta$.

Meanwhile, $\Delta\delta$ was calculated from the lattice expansion coefficient of bulk LSF (ref. [5]) from XRD measurement (Figure 1 in the main text). The experimental conditions for the *in-situ* XPS and *ex-situ* XRD measurements and the quantified $\Delta\delta$ are summarized in **Table S1**.

Table S1. Experimental conditions and the probed oxygen nonstoichiometry change ($\Delta\delta$) for the *in-situ* XPS and *ex-situ* XRD measurement.

	Oxidized state	Reduced state	$\Delta\delta$
In-situ XPS	400 °C, 200 mTorr	300 °C, H_2	~0.3
Ex-situ XRD	As-prepared	400 °C, UHV	~0.3

Supplementary Note 4: La 4*d* and Sr 3*d* spectra

The La 4*d* and Sr 3*d* spectra while heating the LSF sample in H_2 are shown in **Figure S6**. It can be seen that La spectra remained almost unchanged during the heating process, while the concentration of "surface Sr species" [8,9] decreased. The Sr spectra behavior is in accord with the O 1*s* spectra evolution shown in Figure 1 in the main text.

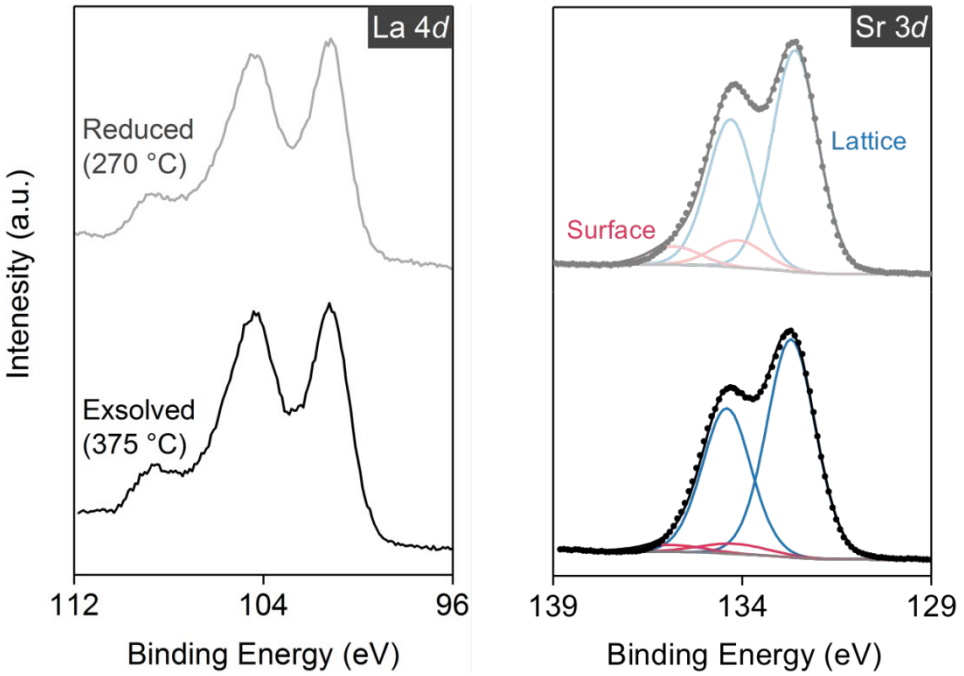

Figure S6. Typical La 4*d* and Sr 3*d* spectra of the LSF surface while heating in 0.5 mbar H_2. Spectrum was collected on LSF/STO with a photon energy of 420 eV.

Supplementary Note 5: Cation and anion diffusion during exsolution

Figure S7 displays a comparison of Fe and O diffusion in an LSF-related perovskite: $La_{0.6}Sr_{0.4}CoO_3$. The blue points represent the Fe/Co interdiffusion[10] while the red and yellow points denote the chemical diffusion[11] and tracer diffusion[12] of O, respectively. As illustrated, anion diffusion is many orders of magnitude faster than that of the cations.

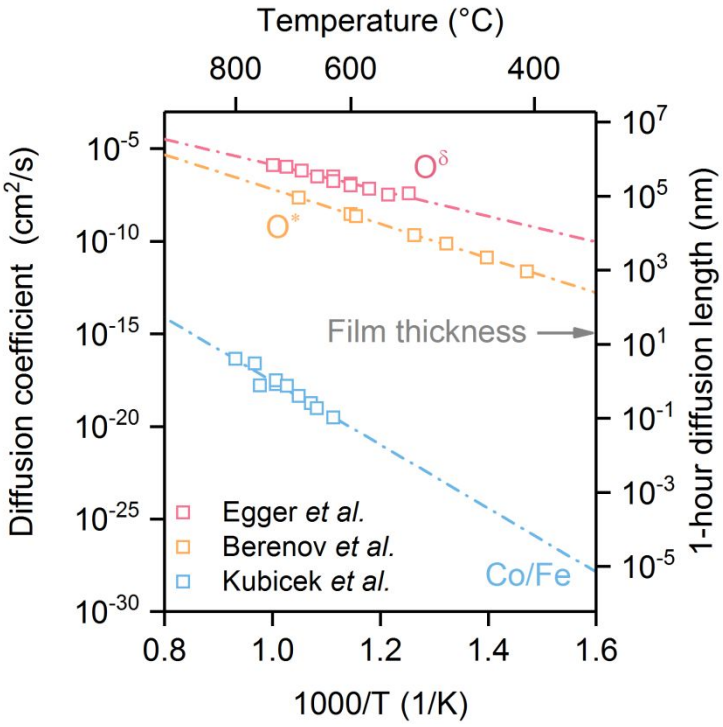

Figure S7. Arrhenius-type plot of the anion and cation diffusion coefficients in $La_{0.6}Sr_{0.4}CoO_3$. The scattered data points are replotted from Ref. [10-12], and the dashed lines represent the linear extrapolation. The right axis shows the corresponding diffusion lengths for 1-hour diffusion time.

With linear extrapolation, we can estimate the characteristic diffusion lengths (l) of Fe and O at 400 °C (i.e., the exsolution temperature used in this work) according to $l = \sqrt{Dt}$, where t represents the diffusion time. In accord with the exsolution conditions used in this work, we set t to be 1 hour. As shown in **Figure S7**, the characteristic chemical and tracer diffusion length for O is around 1×10^4 and 8×10^2 nm, respectively. On the other hand, the characteristic interdiffusion length for Fe is around 7×10^{-5} nm.

Since the characteristic chemical diffusion length for O is much larger than the film thickness (20 nm), the oxygen vacancy formation can take place across the entire LSF film. As a result, bulk chemical expansion has been observed for the LSF film after the mild reduction step (Figure

1f). On the other hand, the formation of Schottky disorder requires a simultaneous displacement of O and Fe to the surface. The small diffusion length of Fe may restrict the Schottky defect formation to the LSF surface under the current exsolution condition. This likely non-uniform defect formation could also explain why no apparent lattice changes was observed upon exsolution (Figure 1f). Nevertheless, further studies are required to validate this hypothesis by measuring the chemical diffusion coefficient of Fe in LSF.

Supplementary Note 6: Quantification of lattice strain

The biaxial lattice strain of the LSF thin films is calculated as

$$strain = \frac{\Delta a}{a} = \frac{a(\text{strained}) - a(\text{relaxed})}{a(\text{relaxed})} \times 100\%$$

where a indicates the pseudo-cubic[10] lattice parameter of the LSF film.

The relaxed lattice parameter is obtained on a thick LSF thin film (~150 nm) grown on MgO (001) substrate, denoted as LSF/MgO. The validity of using this sample to represent the relaxed LSF is shown in **Figure S8**. For a strained film, while the substrate and film peaks can be clearly differentiated in the out-of-plane scan, only one reflection peak is visible in the in-plane scan. This asymmetry is a characteristic of strained films as the film maintains the same in-plane lattice constant as that of the substrate. On the LSF/MgO sample, in both in-plane and out-of-plane XRD scans the substrate and thin film reflex are well-separated and show identical diffraction angles, which suggests that the thick LSF film grown on MgO substrate is fully relaxed. A similar approach to obtain fully relaxed films has also been reported elsewhere[11].

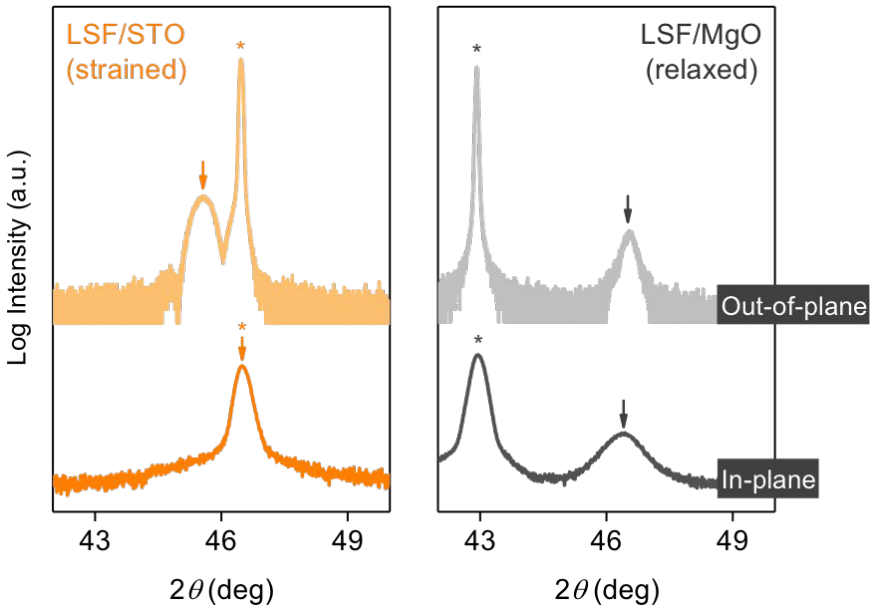

Figure S8. Comparison of the out-of-plane and in-plane XRD on strained (LSF/STO) and relaxed (LSF/MgO) LSF film, where the substrate and LSF peaks are indicated with "*" and arrow, respectively. The in-plane measurement was collected at 1 deg incidence angle. The reflection peak for the in-plane measurement is broader as the in-plane measurement was collected with a parabolic multilayer mirror while the out-of-plane scan was collected with a 2 bounce Ge(022) monochromator.

Due to chemical lattice expansion, however, the relaxed lattice constant $a(\mathrm{relax})$ will evolve during the exsolution process[12]. As a result, the overall strain state of the film will also change during exsolution. To better estimate the lattice strain at the exsolution condition, we measured the lattice parameter of the LSF/MgO after exsolution (3% H_2/N_2 at 650 °C for 5 hours) at room temperature, and the results are summarized in **Table S2**.

Table S2. Summary of the in-plane lattice strain at room temperature induced by lattice misfit.

Sample	In-plane lattice constant	Strain after exsolution
LSF/LSAT	3.87 Å	-1.3 %
LSF/STO	3.91 Å	-0.3 %
LSF/KTO	3.99 Å	+1.8 %
LSF/MgO	3.92 Å	--

Besides, the LSF films will also experience a thermal strain due to the different thermal expansion coefficients between the films and the substrate[13]. The thermal strain for the LSF thin films at the exsolution temperature (i.e., 400 °C) is summarized in **Table S3**. The thermal expansion coefficients for the single crystal substrates are given by the MTI Corporation, while the coefficient for LSF is taken from Ref. [5].

Table S3. Summary of the in-plane thermal lattice strain.

Sample	Thermal expansion coefficient difference*	Thermal strain at 400 °C
LSF/LSAT	$-1 \times 10^{-6}\ K^{-1}$	-0.04 %
LSF/STO	$-1 \times 10^{-6}\ K^{-1}$	-0.04 %
LSF/KTO	$-6 \times 10^{-6}\ K^{-1}$	-0.24 %

As can be seen, the thermal strain is usually an order of magnitude smaller than the strain induced by lattice misfit. Therefore, the majority of the strain inside the LSF films during exsolution is from lattice misfit. Moreover, although the strain states of the thin films may vary during exsolution, the three samples used in this work clearly represent LSF films at three different strain states: compressive, nearly stress-free, and

tensile. Since the aim of this work is to qualitatively compare the exsolution behavior of differently-strained LSF thin films rather than to establish a quantitative relationship, minor deviations from the nominal strain values are expected to be negligible.

Supplementary Note 7: DFT calculation for the strain-dependent defect formation

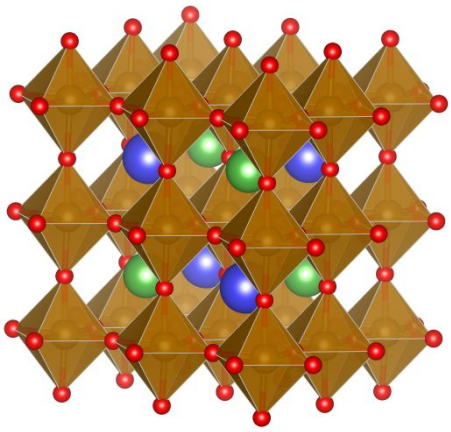

Figure S9. Bulk LSF structure calculated by DFT with alternating La and Sr atoms in the AO termination Green, blue, yellow, and red spheres represent La, Sr, Fe, and O atoms respectively.

Figure S9 shows the bulk 2×2×2 $La_{0.5}Sr_{0.5}FeO_3$ cell used to calculate defect formation energies under biaxial strain. La and Sr cations are arranged in an alternating pattern. As such, the relaxed cell deviates from cubic structure, with lattice parameter of 3.66 Å in the *a* direction, and 3.89 Å in the *b* and *c* directions. The strain-dependent defect formation energies are calculated by applying biaxial strain on the *bc* plane.

Supplementary Note 8: More Characterizations of the NAP-XPS sample

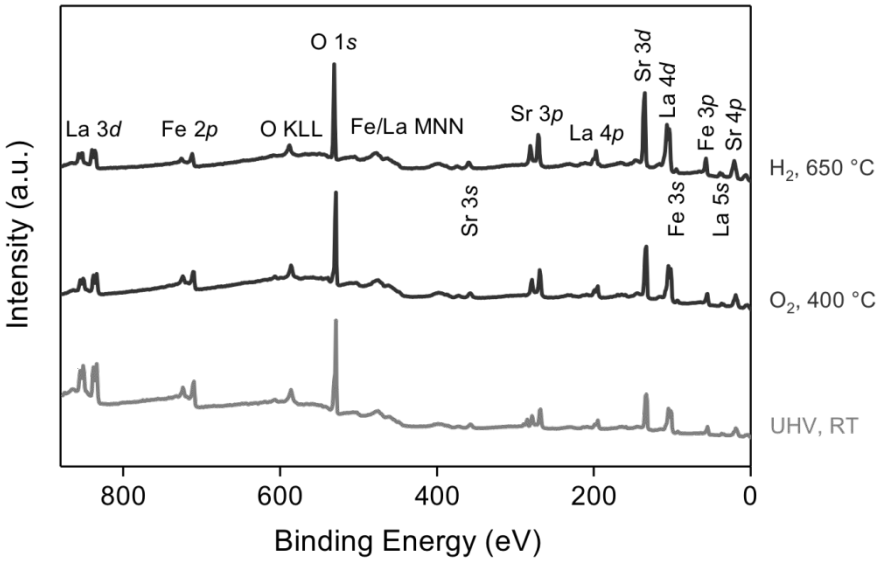

Figure S10. Surface chemistry of LSF thin films. Typical NAP-XPS survey scan of the LSF thin films collected under various conditions, where only La, Sr, Fe, and O signals are observed. Spectra were collected at a photon energy of 1010 eV.

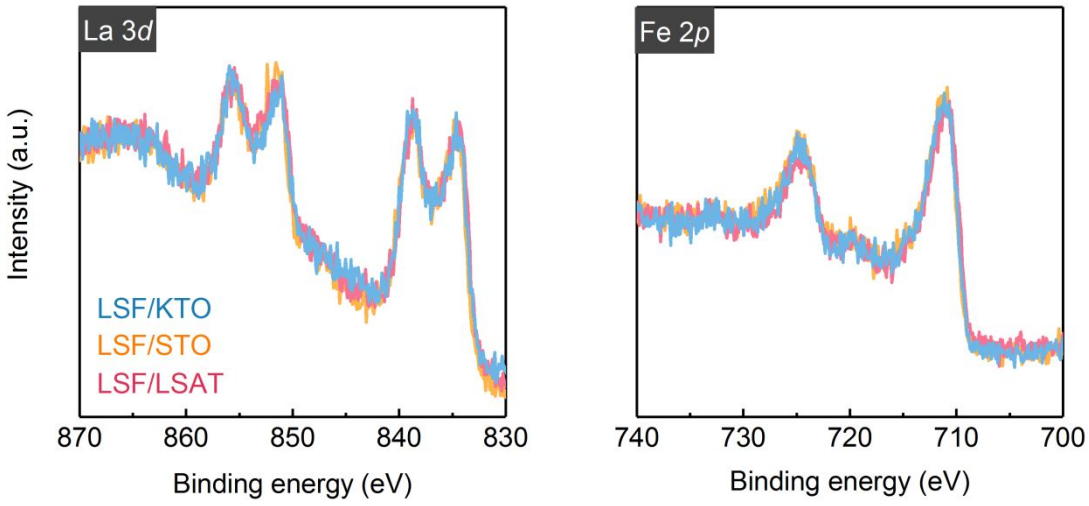

Figure S11. Similar La 3*d* and Fe 2*p* XPS spectra of the as-prepared LSF films grown on different substrates.

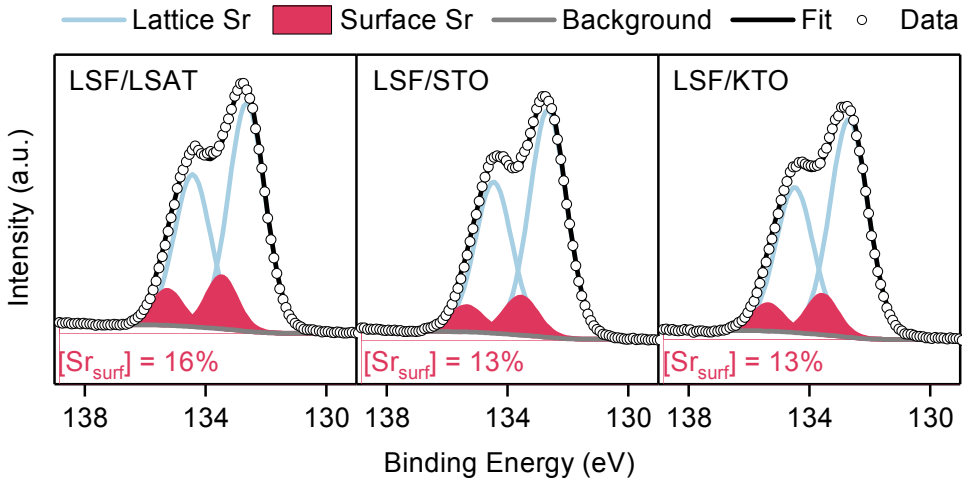

Figure S12. Sr 3*d* spectra of the LSF thin films at the exsolution condition, where no apparent strain dependency has been observed. The Sr 3*d* spectra are deconvoluted into surface and lattice Sr components, where a detailed fitting method can be found in the Ref. [8]. Spectra are collected at 400 °C in 0.5 mbar H_2 with a photon energy of 420 eV.

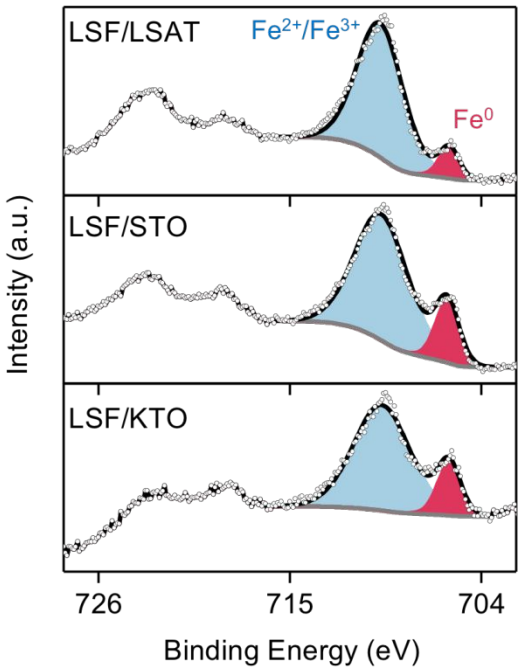

Figure S13. Fe 2*p* spectra of the LSF thin film at the exsolution condition, where the Fe 2$p_{3/2}$ are deconvoluted into Fe^{2+}/Fe^{3+} and Fe^0 species. As can be seen, for LSF/KTO, the Fe^0 concentration cannot be simply estimated with the Fe 2$p_{3/2}$ as the overall Fe 2p spectra profile also changed. To avoid the complexity in peak shape, Fe 3*p* are used for [Fe^0] estimation. Spectra are collected at 400 °C in 0.5 mbar flushing H_2 with a photon energy of 862.7 eV.

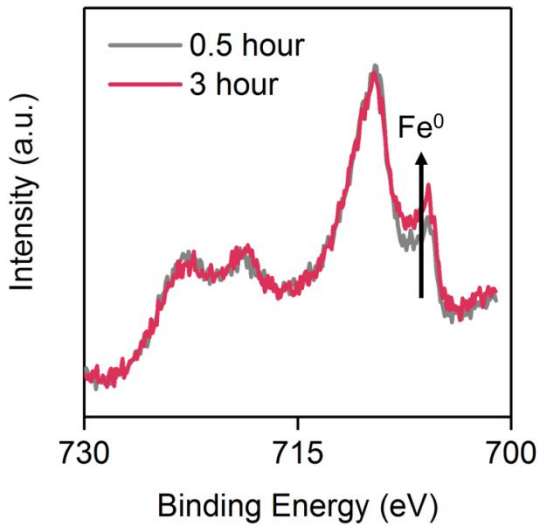

Figure S14. Time-dependent Fe 2*p* spectra shows the LSF surface is not equilibrated after 30 minutes of exsolution. Spectra were collected at 400 °C in 0.5 mbar flushing H_2 with a photon energy of 862.7 eV on LSF/STO.

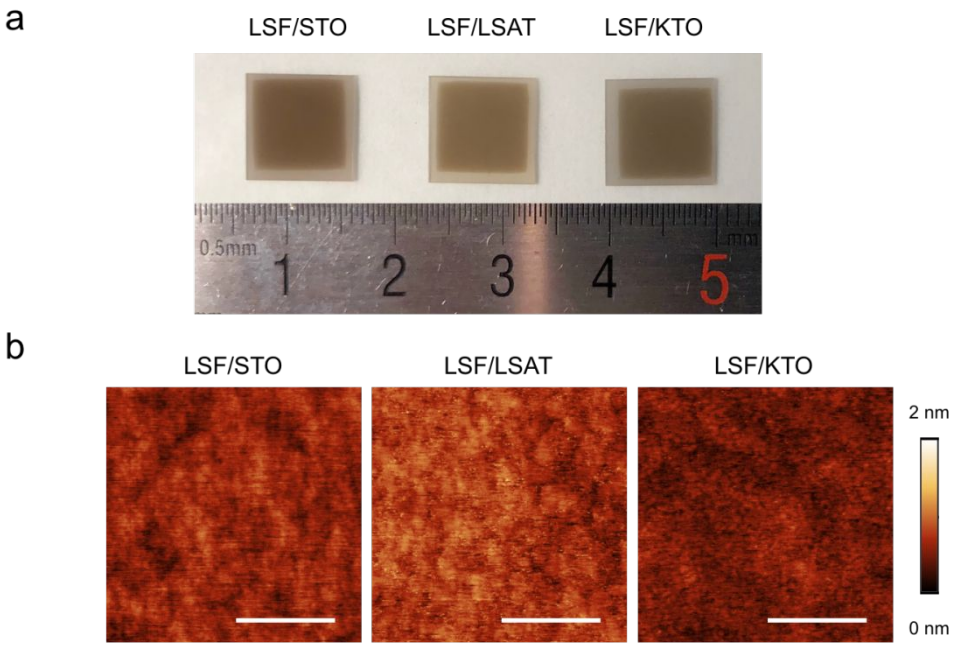

Figure S15. Sample morphology. **(a)** Optical image of the as-prepared LSF thin films. **(b)** Atomic force microscopy (AFM) image of the as-prepared LSF surface. Scale bar: 400 nm.

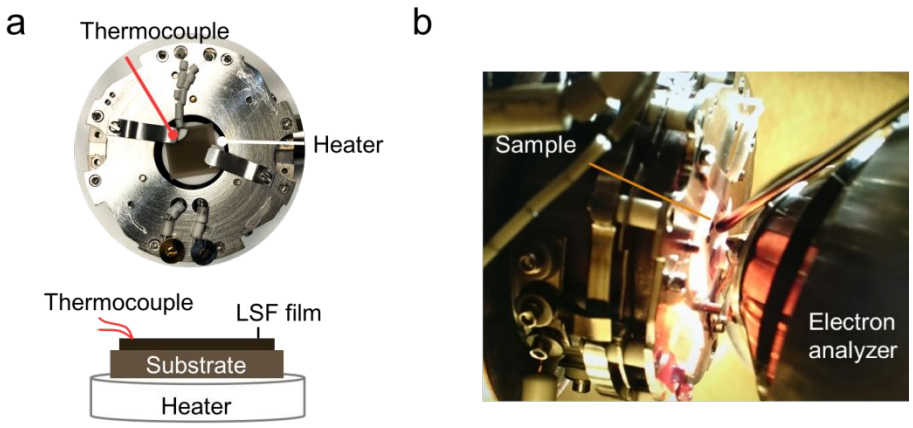

Figure S16. The APXPS experimental setup. (a) Photo and sketch of the APXPS sample holder. The thermocouple is placed on top of the LSF thin film during the measurement. (b) Photo showing the sample holder during the APXPS measurement.

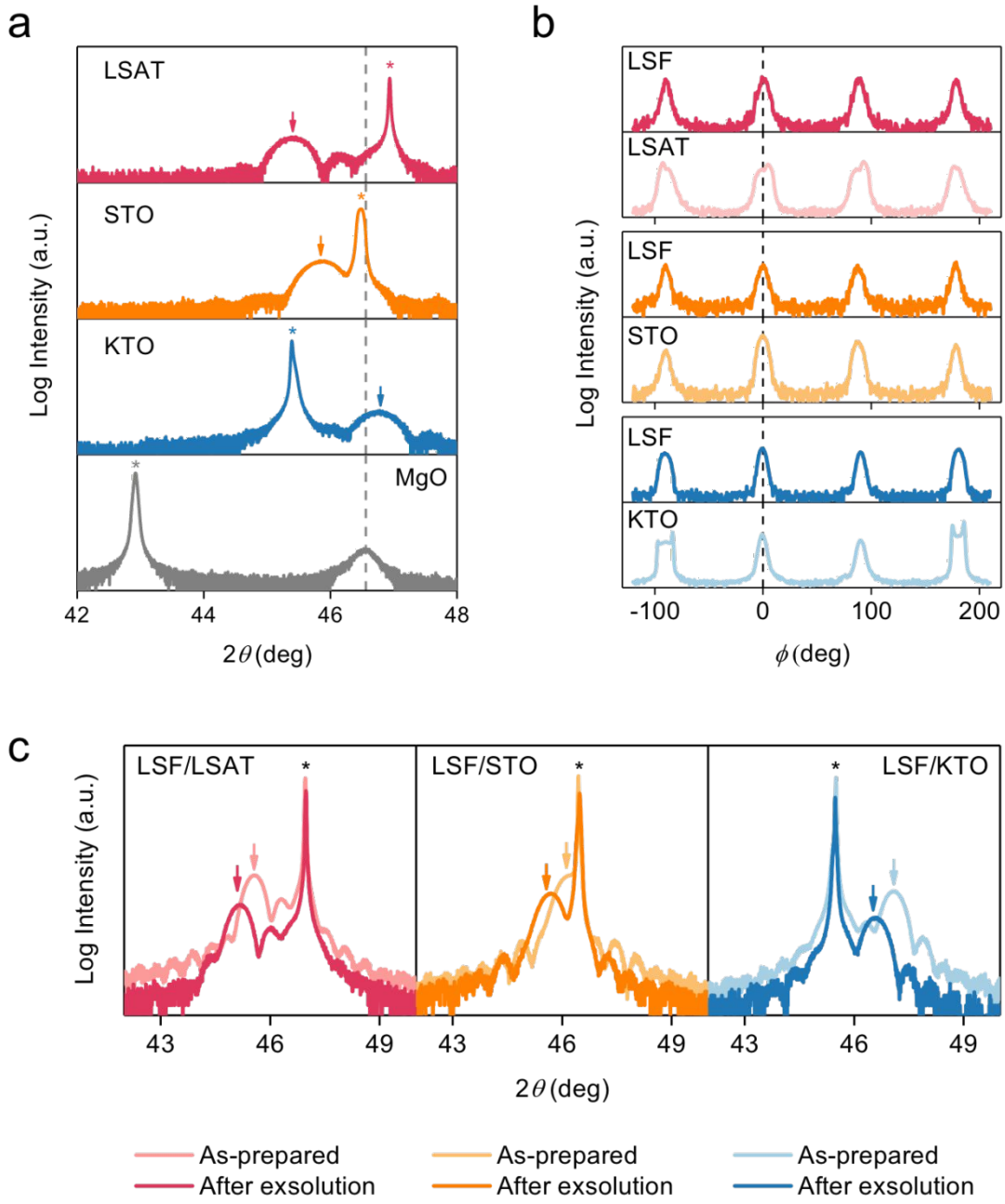

Figure S17. Lattice structure of the LSF thin films. **(a)** Out-of-plane symmetric 2θ-ω X-ray diffraction scan at the pseudo-cubic (002) reflection of the as-prepared LSF thin films, where the dotted line indicates the peak position of the relaxed LSF film grown on MgO substrate. Due to the in-plane lattice strain, LSF/ KTO and LSF/STO have smaller out-of-plane lattice spacing while LSF/LSAT has a larger out-of-plane lattice constant. **(b)** Phi-scan about the pseudo-cubic (103) reflection, confirming the cube-on-cube alignment of the LSF films on LSAT, STO, and KTO substrates. **(c)** Out-of-plane symmetric 2θ-ω X-ray diffraction scan highlights the lattice expansion during film reduction and Fe^0 exsolution. LSF and substrate peaks are indicated with arrow and asterisk, respectively.

Table S4. Bulk chemistry of LSF thin films. **(a)** Thin-film and **(b)** powder LSF composition obtained from inductively-coupled plasma mass spectrometry (ICP- MS). Note the both LSF thin films and LSF powders (the raw material for PLD target) show a bulk chemistry close to the ideal composition $La_{0.6}Sr_{0.4}FeO_3$.

a

Thin-film	La/Fe	Sr/Fe	A:B
1	0.62	0.38	1.03
2	0.63	0.37	1.04
3	0.63	0.37	1.04
4	0.61	0.39	0.95
5	0.62	0.38	1.06
6	0.61	0.39	0.95
7	0.61	0.39	1.00
8	0.63	0.37	1.01
9	0.58	0.42	1.03
Average	0.62 ± 0.02	0.38 ± 0.02	1.01 ± 0.04

b

Powder	La/Fe	Sr/Fe	A:B
1	0.58	0.42	1.03
2	0.60	0.40	0.99
3	0.60	0.40	1.00
Average	0.59 ± 0.01	0.41 ± 0.01	1.01 ± 0.02

Supplementary Note 9: AFM imaging and quantification

The vertical resolution (Δz) of AFM is mainly limited by the thermal noise, and can be estimated as[14]:

$$\Delta z = \sqrt{\frac{4k_{\mathrm{B}}T}{3k}} \approx 0.01 \text{ nm},$$

where k_B is the Boltzmann constant, and k is the spring constant of the cantilever. Here k is taken as 40 N/m for the Bruker TESP-V2 probe, and T is 300 K as room temperature.

Meanwhile, tip sharpness mainly determines the lateral resolution (d) of AFM. As schematically shown in **Figure S18**a, the lateral resolution is defined as the minimum detectable distance between two sharp features, which is given by[14]:

$$d = \sqrt{2R}\left(\sqrt{\Delta z} + \sqrt{\Delta z + \Delta h}\right),$$

where R is the tip radius and Δh is the relative height difference of the two features. Here the tip radius is taken as 7 nm for the Bruker TESP-V2 probe. As a result, the ideal lateral resolution at a fixed vertical resolution $\Delta z = 0.01$ nm is shown in **Figure S18**b, where the resolution regime is highlighted in gray.

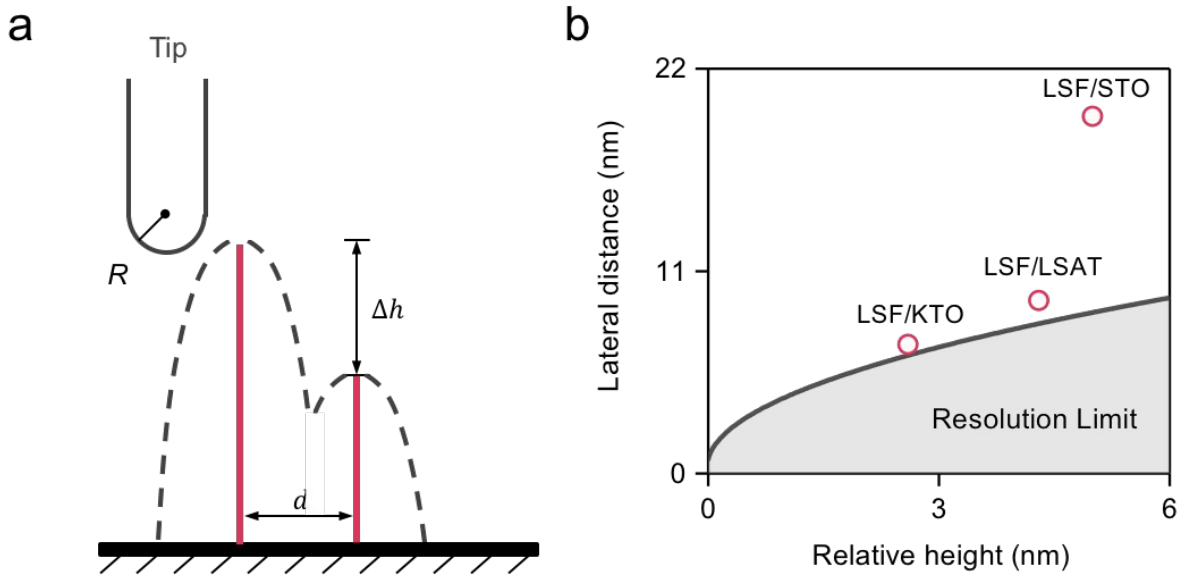

Figure S18. AFM lateral resolution. **(a)** Sketch of an AFM scan over two spikes of different heights (Δh) with a lateral distance d. The dashed line indicates the apparent surface morphology in AFM. **(b)** Comparison between the theoretical lateral resolution and the experimentally observed particle sizes. The "invisible" regime due to the resolution limit is highlighted in gray, whereas the mode particle size of differently-strained LSF films are shown for comparison.

As can be seen, the mode values of the particle sizes in this study are within the AFM capability. Nevertheless, the particle sizes on the tensile-strained LSF (LSF/KTO) surface is approaching the resolution limit, which makes it very challenging to precisely estimate the particle size. To confirm the surface morphology of the LSF/KTO, we conducted the AFM measurement with two types of AFM tips and the results are shown in **Figure S19**. As can be seen, the particle sizes obtained from the two AFM tips are pretty similar. Therefore, we expect the AFM images to represent the real surface morphology in our study.

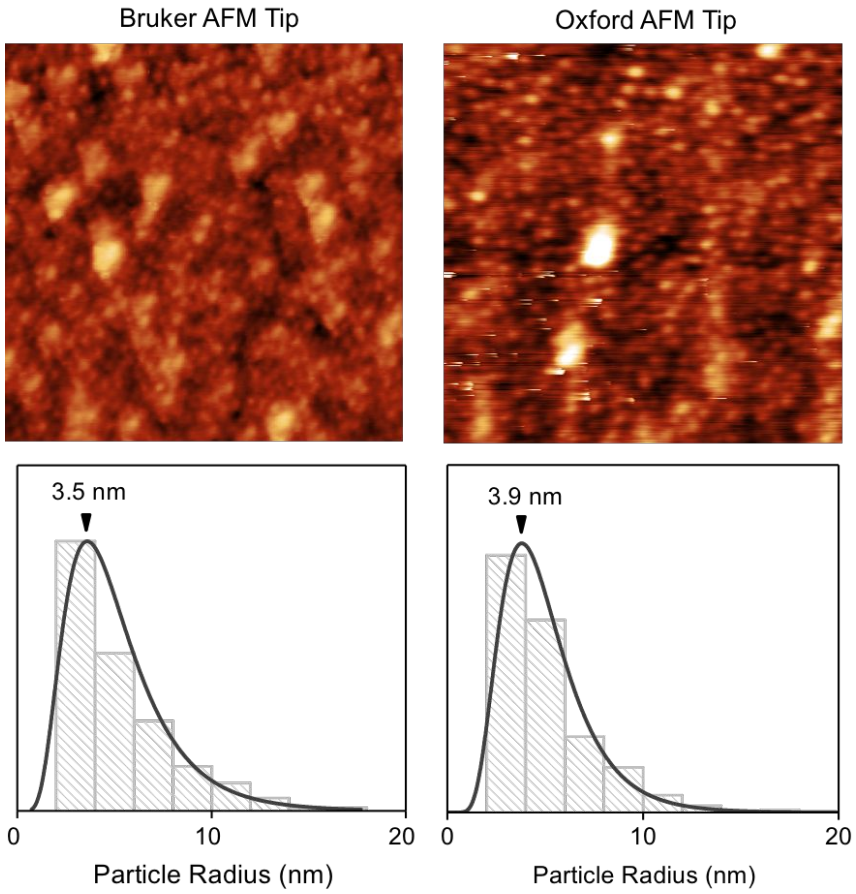

Figure S19. Tip effect on the AFM images. The AFM images were collected on LSF/KTO sample with two AFM tips: Bruker TESP-V2 and Oxford AC160TS-R3.

A watershed algorithm is implemented to mark the particles with Gwyddion software, where the parameter settings are summarized in **Table S5** and the particle marking results are shown in **Figure S20**.

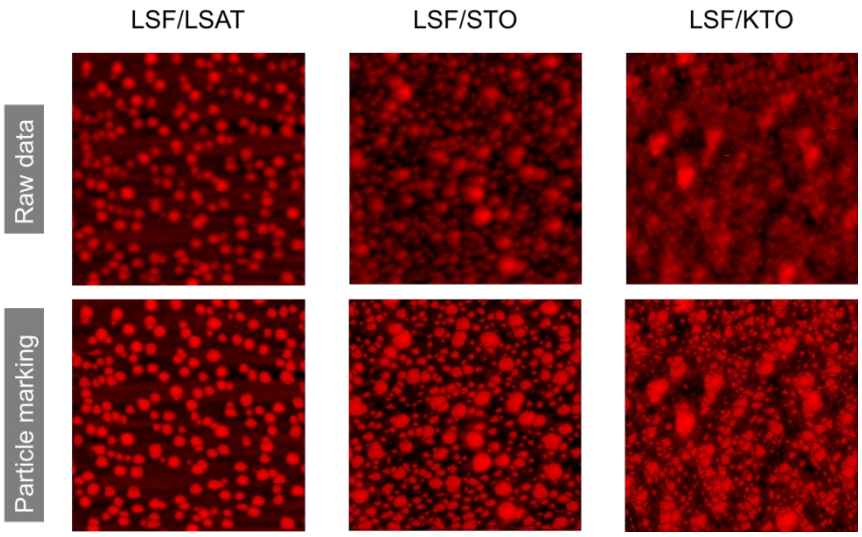

Figure S20. Particle marking results of the AFM images from Gwyddion with watershed algorithm.

Table S5. Parameter setting for the watershed algorithm in Gwyddion.

Grain Location	
Number of steps	10
Drop size	0.5%
Threshold	0
Segmentation	
Number of steps	50
Drop size	5%

After the initial particle marking, a filter of 4 pixel areas (corresponding to ~ 15 nm^2) was employed to the marked particles. In other words, only particles with projected area larger than 4 pixels are considered in the data analysis. **Figure S21** depicts the relation between the area filter threshold and the obtained particle density. Clearly, the obtained particle density is sensitive to this threshold filter, and its error bar is then estimated from the standard deviation of the quantity obtained from a threshold between 2 to 6 pixels.

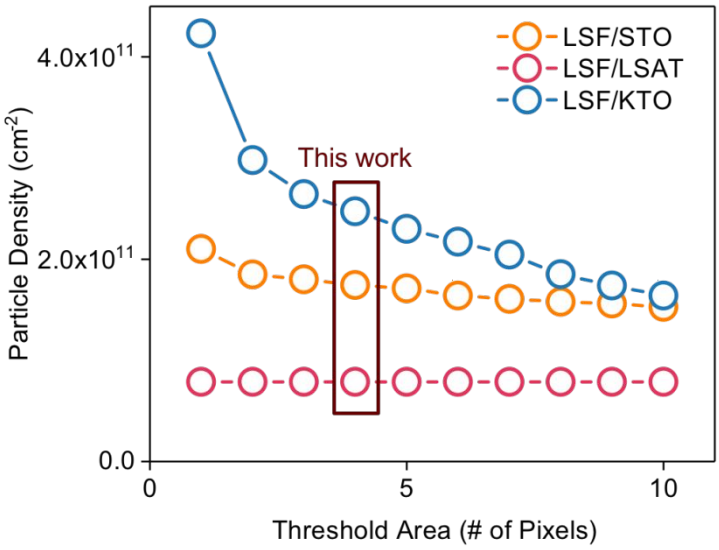

Figure S21. Sensitivity analysis of the particle density as a function of the threshold area filter. In this work, only particles with a projected area larger than 4 pixels are considered in the data analysis.

Histograms of the equivalent disk radius is produced with Origin by splitting the data range from 0 to 20 nm into 20 bins of equal size. Each histogram is fitted with a distribution curve to obtain the mode number. The distribution curves used for the LSF/LSAT, LSF/STO, and LSF/KTO are Weibull, Lognormal, and Lognormal, respectively.

Supplementary Note 10: Strain-dependent Fe^0 exsolution in UHV

Besides the results shown in Figure 4 in the main text, we further examined the strain-dependent Fe^0 exsolution in UHV condition. In this study, the LSF film were grown onto two (001)-oriented perovskite-type single crystal substrates with different lattice parameters: $LaAlO_3$ (LAO) and $SrTiO_3$ (STO). These two LSF films are denoted with LSF/LAO and LSF/STO, respectively. The corresponding reciprocal space maps (RSM) for these two samples are shown in **Figure S22**. As illustrated, the film peak for LSF/STO is directly above that of the substrate, meaning that the LSF thin films maintained identical in-plane lattice parameter as that of the substrates. On the other hand, the LSF/LAO film shows partial relaxation due to the large lattice mismatch. Nevertheless, the two samples used here clearly represent LSF films with two different strain states: compressive (LSF/LAO), and nearly stress-free (LSF/STO). These two samples were heated in UHV chamber and monitored with *in-situ* XPS. As illustrated in **Figure S23**a, the LSF/STO sample exhibited an early exsolution onset compared to LSF/LAO. The onset difference thus indicates that the exsolution phenomena in LSF/LAO was suppressed by the large compressive strain. In accord with the XPS characterization, AFM measurements (**Figure S23**b) also revealed a higher particle density in the LSF/STO surface compared to LSF/LAO after exsolution.

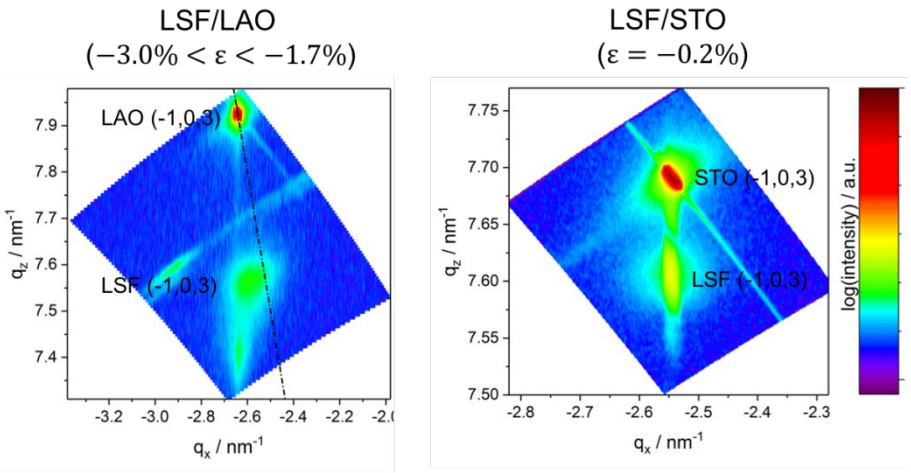

Figure S22. X-ray RSM about the (103) reflection of the LSF thin films. Note the LSF/LAO film is partially relaxed, where the dashed line indicates the location of a completely relaxed film. The numbers in the parenthesis indicate the in-plane strain in these two films, where negative values indicate compressive strains.

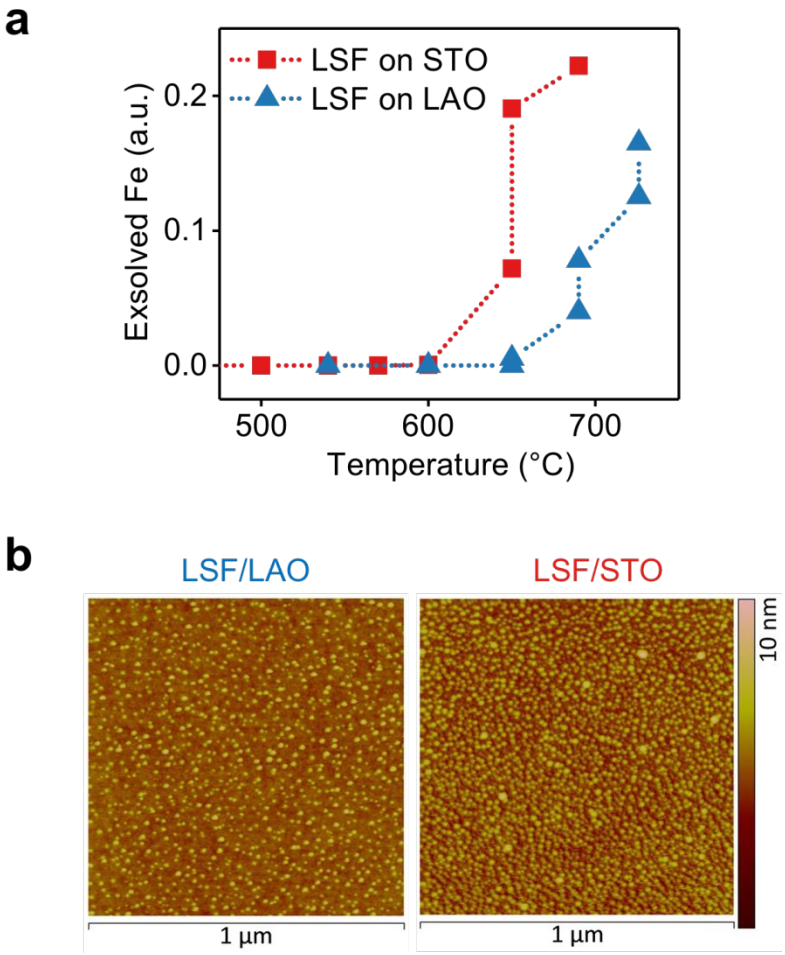

Figure S23. Strain-dependent Fe^0 exsolution in UHV condition. (**a**) Temperature-dependent surface concentration of Fe^0 while heating in UHV. Note the LSF/STO sample has an early exsolution onset than LSF/LAO. (**b**) AFM analysis of the two LSF samples after exsolution, where LSF/STO shows a much higher particle density than the LSF/LAO.

Supplementary Note 11: Summary of lattice volume change in exsolution

Parent Oxide	Exsolved Metal	Volume Change*	Reference
$La_{0.85}Sr_{0.15}CrO_3$	Pd	+	[15]
$La_{0.6}Sr_{0.4}FeO_3$	Fe	+	[16]
$La_{0.4}Sr_{0.4}ScO_3$	Ni	+	[17]
$LaFe_{0.57}Co_{0.38}O_3$	Pd	+	[18]
$Sr_{0.94}Ti_{0.9}Nb_{0.1}O_3$	Ni	+	[19]
$La_{0.5}Sr_{0.5}TiO_3$	Ni	+	[20]
$Sr_{0.95}Ti_{0.3}Fe_{0.7}O_3$	Ni	+	[21]
$La_{0.4}Sr_{0.4}TiO_3$	Ni, Fe	+	[22]
$(La_{0.2}Sr_{0.8})_{0.9}TiO_3$	Fe	-	[23]
$(Sr_{0.7}Pr_{0.3})_{0.9}TiO_3$	Ni	-	[24]
$La_{0.2}Sr_{0.7}TiO_3$	Ni	-	[25]
$La_{0.2}Sr_{0.7}TiO_3$	Ni	+/- (mixed)	[26]
$La_{0.2}Sr_{0.8}TiO_3$	Ni	+/- (mixed)	[27]
$La_{0.4}Sr_{0.4}TiO_3$	Fe, Ni, Co	+/- (mixed)	[28]

* "+" stands for the volume expansion, while "−" represents contraction.

Supplementary Note 12: Characterization of the atomically-flat LSF surface

The morphology of the as-prepared LSF surface is shown in **Figure S24**a. As illustrated, the step-and-terrace morphology is present with an average step height of ~0.38 nm. This step height corresponds to the unit cell height of LSF. To reveal the surface structure, low-energy electron diffraction (LEED) patterns were collected on the LSF films that are grown on the Nb:STO (001) substrate using the same PLD deposition condition. The Nb:STO substrate was employed to increase the sample electrical conductivity. As shown in **Figure S24**b, the as-prepared LSF surface has a four-fold symmetry, in agreement with the (001) cubic surface structure. The surface chemistry and morphology evolution during heating in UHV is shown in **Figure S25**.

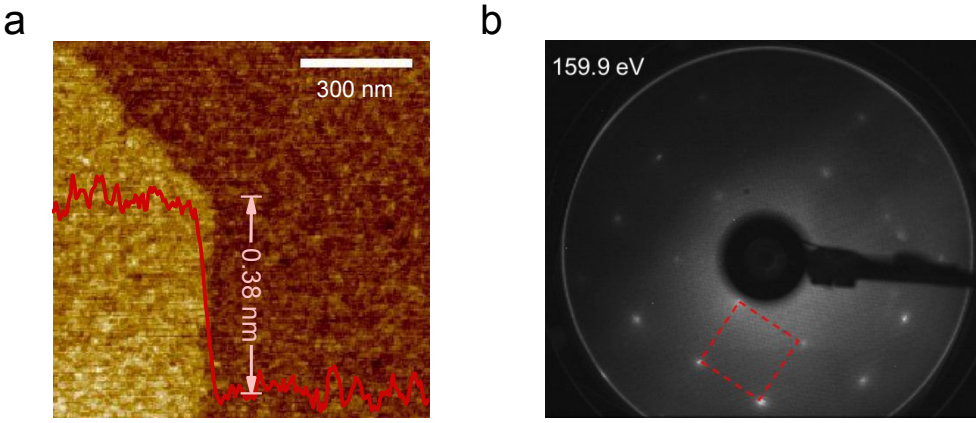

Figure S24. Characterization of the as-prepared LSF (001) surface. (**a**) AFM image of the as-prepared LSF film. Inset: line scan showing the step height to be ~ 0.38 nm. (**b**) Low-energy electron diffraction patterns for the LSF film, using 159.9 eV electrons. A fourfold symmetry highlighted by the dashed square.

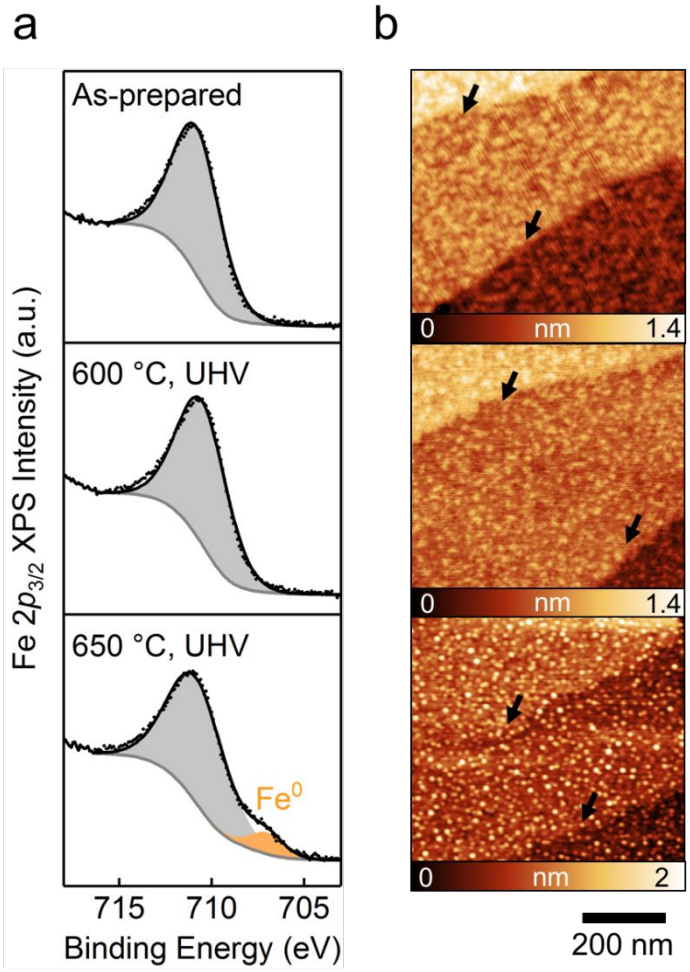

Figure S25. (**a**) *In situ* XPS and (**b**) *ex situ* AFM images of an atomically-flat LSF (001) thin film at different stages of exsolution: as-prepared, reduced, and exsolved. The arrows in (b) indicate the locations of the atomic steps.

Supplementary Note 13: Comparison between isolated $V_O^{\bullet\bullet}$ and $V_O^{\bullet\bullet}$ pair

Based on a two-level system, we estimated the fraction of Fe adatoms and Fe dimers adsorbed on isolated $V_O^{\bullet\bullet}$ versus to $V_O^{\bullet\bullet}$ pairs. The fraction is calculated as:

$$f = \left[1 + e^{-\frac{\Delta E}{kT}}\right]^{-1},$$

where k represents Boltzmann constant, and ΔE denotes the binding energy difference the isolated $V_O^{\bullet\bullet}$ and $V_O^{\bullet\bullet}$ pairs. The results are shown in **Figure S26**. According the DFT calculation (Figure 6), ΔE is set to be 0.52 eV and 0.15 eV for Fe and Fe_2 adsorption, respectively. As illustrated, we expect more than 99% of the Fe adatoms and more than 80% of the Fe dimers will stick to $V_O^{\bullet\bullet}$ pairs compared to isolated $V_O^{\bullet\bullet}$ under exsolution conditions.

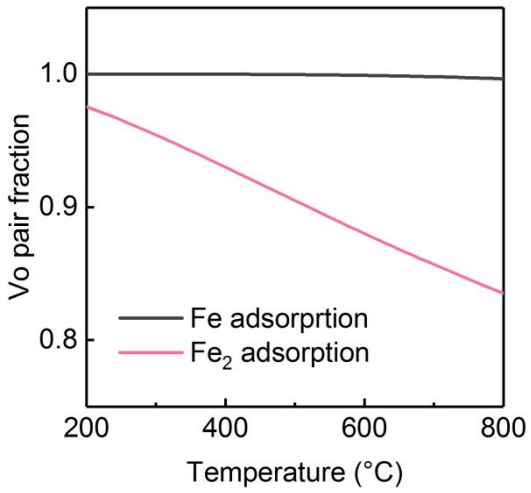

Figure S26. Fraction of Fe and Fe_2 adsorbed on $V_O^{\bullet\bullet}$ pairs as a function of temperature. The two solid lines are calculated with $\Delta E = 0.15$ eV and $\Delta E = 0.52$ eV for Fe and Fe_2 adsorption, respectively.

Reference

1. Nenning, A. & Fleig, J. Electrochemical XPS investigation of metal exsolution on SOFC electrodes: Controlling the electrode oxygen partial pressure in ultra-high-vacuum. *Surface Science* **680,** 43–51 (2019).
2. Nenning, A. *et al.* Ambient Pressure XPS Study of Mixed Conducting Perovskite-Type SOFC Cathode and Anode Materials under Well-Defined Electrochemical Polarization. *J. Phys. Chem. C* **120,** 1461–1471 (2016).
3. Chen, M., Hu, Y., Chen, D., Hu, H. & Xu, Q. A novel anode for solid oxide fuel cells prepared from phase conversion of La0.3Sr0.7Fe0.7Cr0.3O3-δ perovskite under humid hydrogen. *Electrochimica Acta* **284,** 303–313 (2018).
4. Mueller, D. N., Machala, M. L., Bluhm, H. & Chueh, W. C. Redox activity of surface oxygen anions in oxygen-deficient perovskite oxides during electrochemical reactions. *Nature Communications* **6,** 6097 (2015).
5. Kuhn, M., Hashimoto, S., Sato, K., Yashiro, K. & Mizusaki, J. Oxygen nonstoichiometry, thermo-chemical stability and lattice expansion of La0.6Sr0.4FeO3 − δ. *Solid State Ionics* **195,** 7–15 (2011).
6. Gopal, C. B., Gabaly, F. E., McDaniel, A. H. & Chueh, W. C. Origin and Tunability of Unusually Large Surface Capacitance in Doped Cerium Oxide Studied by Ambient-Pressure X-Ray Photoelectron Spectroscopy. *Advanced Materials* **28,** 4692–4697 (2016).
7. Hofmann, S. *Auger- and X-Ray Photoelectron Spectroscopy in Materials Science*. **49,** (Springer Science & Business Media, 2012).
8. Crumlin, E. J. *et al.* Surface strontium enrichment on highly active perovskites for oxygen electrocatalysis in solid oxide fuel cells. *Energy Environ. Sci.* **5,** 6081–6088 (2012).
9. Opitz, A. K. *et al.* The Chemical Evolution of the La0.6Sr0.4CoO3−δ Surface Under SOFC Operating Conditions and Its Implications for Electrochemical Oxygen Exchange Activity. *Top Catal* **61,** 2129–2141 (2018).
10. Lee, D. *et al.* Stretching Epitaxial La 0.6Sr 0.4CoO 3−δfor Fast Oxygen Reduction. *J. Phys. Chem. C* **121,** 25651–25658 (2017).
11. Gopal, C. B. *et al.* Equilibrium oxygen storage capacity of ultrathin CeO2-δ depends non-monotonically on large biaxial strain. *Nature Communications* **8,** ncomms15360 (2017).
12. Perry, N. H., Kim, J. J., Bishop, S. R. & Tuller, H. L. Strongly coupled thermal and chemical expansion in the perovskite oxide system Sr(Ti,Fe)O 3−α. *J. Mater. Chem. A* **3,** 3602–3611 (2015).
13. Thompson, C. V. Solid-State Dewetting of Thin Films. *Annu. Rev. Mater. Res.* **42,** 399–434 (2012).
14. Gan, Y. Atomic and subnanometer resolution in ambient conditions by atomic force microscopy. *Surface Science Reports* **64,** 99–121 (2009).
15. Bierschenk, D. M. *et al.* Pd-substituted (La,Sr)CrO3−δ–Ce0.9Gd0.1O2−δ solid oxide fuel cell anodes exhibiting regenerative behavior. *Journal of Power Sources* **196,** 3089–3094 (2011).
16. Götsch, T. *et al.* Crystallographic and electronic evolution of lanthanum strontium ferrite (La 0.6 Sr 0.4 FeO 3−δ) thin film and bulk model systems during iron exsolution. *Physical Chemistry Chemical Physics* **21,** 3781–3794 (2019).
17. Gao, Y., Chen, D., Saccoccio, M., Lu, Z. & Ciucci, F. From material design to mechanism study: Nanoscale Ni exsolution on a highly active A-site deficient anode material for solid oxide fuel cells. *Nano Energy* **27,** 499–508 (2016).
18. Nishihata, Y. *et al.* Self-regeneration of a Pd-perovskite catalyst for automotive emissions control. *Nature* **418,** 164–167 (2002).
19. Yang, L. *et al.* Redox-reversible niobium-doped strontium titanate decorated with in situ grown nickel nanocatalyst for high-temperature direct steam electrolysis. *Dalton Trans.* **43,** 14147–14157 (2014).
20. Arrivé, C., Delahaye, T., Joubert, O. & Gauthier, G. Exsolution of nickel nanoparticles at the surface of a conducting titanate as potential hydrogen electrode material for solid oxide electrochemical cells. *Journal of Power Sources* **223,** 341–348 (2013).
21. Zhu, T., Troiani, H. E., Mogni, L. V., Han, M. & Barnett, S. A. Ni-Substituted Sr(Ti,Fe)O3 SOFC Anodes: Achieving High Performance via Metal Alloy Nanoparticle Exsolution. *Joule* **2,** 478–496 (2018).
22. Tsekouras, G., Neagu, D. & Irvine, J. T. S. Step-change in high temperature steam electrolysis performance of perovskite oxide cathodes with exsolution of B-site dopants. *Energy Environ. Sci.* **6,** 256–266 (2013).
23. Qin, Q. *et al.* Perovskite titanate cathode decorated by in-situ grown iron nanocatalyst with enhanced electrocatalytic activity for high-temperature steam electrolysis. *Electrochimica Acta* **127,** 215–227 (2014).
24. Kamecki, B., Miruszewski, T., Górnicka, K., Klimczuk, T. & Karczewski, J. Characterization methods of nickel nano-particles obtained by the ex-solution process on the surface of Pr, Ni-doped SrTiO3 perovskite ceramics. *SN Applied Sciences* **1,** 322 (2019).
25. Han, H. *et al.* Lattice strain-enhanced exsolution of nanoparticles in thin films. *Nature Communications* **10,** 1471 (2019).
26. Kim, K. J. *et al.* Facet-Dependent in SituGrowth of Nanoparticles in Epitaxial Thin Films: The Role of Interfacial Energy. *J. Am. Chem. Soc.* **141,** 7509–7517 (2019).
27. Park, B. H. & Choi, G. M. Ex-solution of Ni nanoparticles in a La0.2Sr0.8Ti1−xNixO3−δ alternative anode for solid oxide fuel cell. *Solid State*

Ionics **262,** 345–348 (2014).

28. Zhu, Y. *et al.* Synergistically enhanced hydrogen evolution electrocatalysis by in situexsolution of metallic nanoparticles on perovskites. *J. Mater. Chem. A* **6,** 13582–13587 (2018).